

The Impact of Aerosols on the Stratiform Clouds over Southern West Africa: A Large-Eddy Simulation Study

Lambert Delbeke¹, Chien Wang¹, Pierre Tulet¹, Cyrielle Denjean², Maurin Zouzoua³, Nicolas Maury⁴
5 and Adrien Deroubaix⁵

¹Laboratoire d'Aérodynamique, Université de Toulouse, CNRS, UT3, IRD, Toulouse, France

²CNRM, Université de Toulouse, Météo-France, CNRS, Toulouse, France

³Laboratoire Atmosphères, Milieux, Observations Spatiales, IPSL, CNRS, Guyancourt, France

⁴CNRM, Université de Toulouse, Météo-France, CNRS, Toulouse; now at LMD/IPSL, Paris, France

10 ⁵IUP, Institute of Environmental Physics, University of Bremen, Bremen, and Max Plank Institute for Meteorology, Hamburg, Germany

Correspondence to: Chien Wang (chien.wang@aero.obs-mip.fr), Cyrielle Denjean (cyrielle.denjean@meteo.fr)

Abstract. The low level stratiform clouds (LLSCs) covering a large area appear frequently during the wet monsoon season in southern West Africa. This region is also a place where different types of aerosols
15 coexist, including the biomass burning aerosols coming from Central and South Africa and the aerosols emitted by local anthropogenic activities. We investigate the indirect and semi-direct effects of these aerosols on the life cycle of LLSCs by conducting a case study based on the airborne and ground-based observations from the field campaign of Dynamic-Aerosol-Chemistry-Cloud-Interaction in West Africa (DACCIIWA). This case is modeled using a Large Eddy Simulation (LES) model with fine resolution and
20 in-situ aerosol measurements including size distribution and chemical composition. The model has successfully reproduced the observed life cycle of the LLSC, from stratus formation to stabilization during the night, and to the upward development after sunrise until break-up of cloud deck in the late afternoon. Additional sensitivity simulations using different measured aerosol profiles also suggest that aerosols can affect the cloud life cycle through both the indirect and semi-direct effect. As expected,
25 modeled cloud microphysical features including cloud droplet number concentration, mean radius, and thus cloud reflectivity are all controlled by aerosol concentration. However, it is found that the difference variation in cloud reflectivity induced by different aerosol profiles is not always the only factor in determining the ~~variation-of-the~~ incoming solar radiation at ground and thus cloud life cycle after sunrise. Instead, the difference in cloud fraction brought by dry air entrainment from above and thus the speed of
30 consequent evaporation - also influenced by aerosol concentration, is another important factor to consider. Clouds influenced by higher aerosol concentrations and thus having higher number concentration and smaller sizes of cloud droplets are found to evaporate more easily and thus impose a lower cloud fraction. In addition, we find that an excessive atmospheric heating up to $12 K day^{-1}$ produced by absorbing black carbon aerosols (BC) in our modeled cases ~~can lower~~
35 resulting a weaker extent in vertical development while a higher cloud fraction, ~~and~~ and delaying intense cloud break-up until-before later afternoon, ~~making a positive contribution to the indirect effect~~. While the ~~resulted~~ thinner clouds resulted from such a heating, on the other hand, would break up faster in late afternoon when convection is further strengthened, thus contributing negatively to the indirect effect.

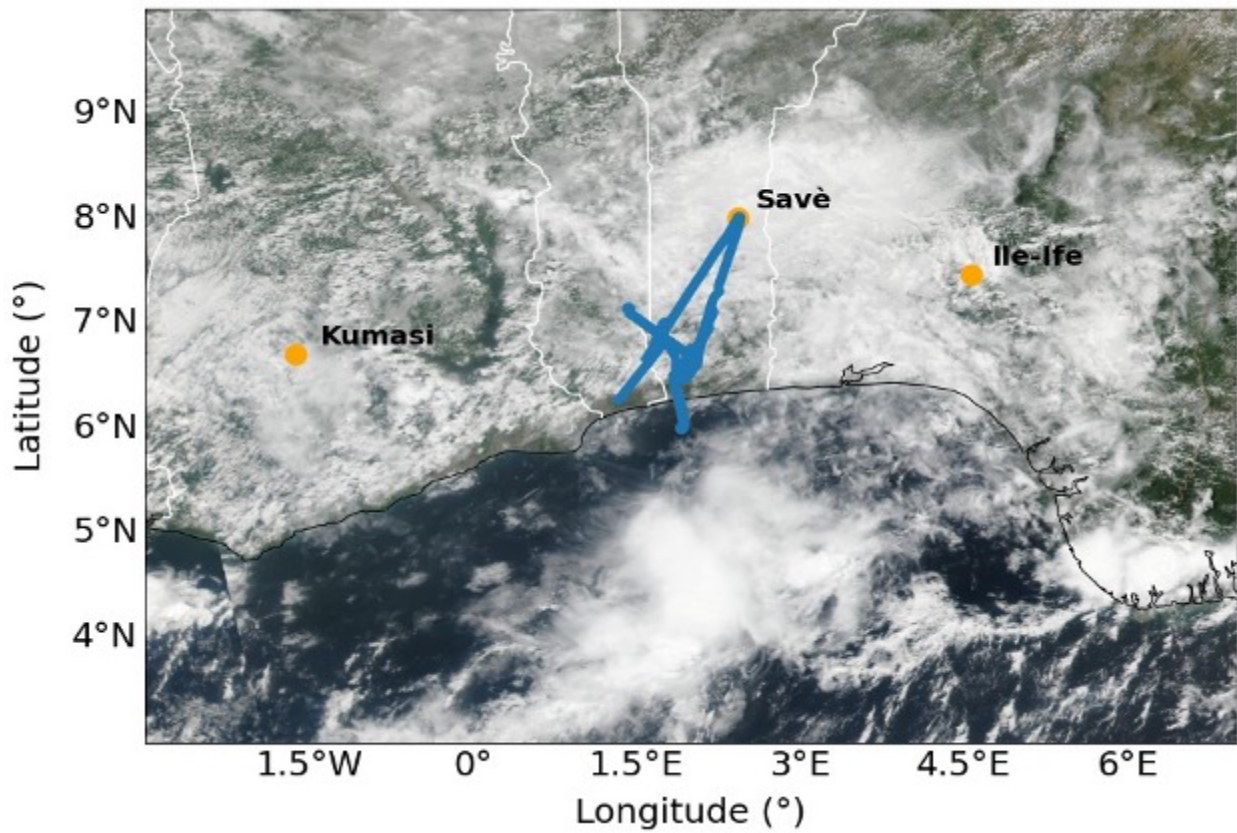
40 1. Introduction

Low-level stratiform clouds (LLSCs) have a higher albedo and a larger cloud ~~deck covering Earth's surface cover~~ than many other types of clouds (Hartmann *et al.*, 1992; Chen *et al.*, 2000; Eastman and Warren, 2014). Their reflection of solar radiation is thus important to Earth's radiative budget. LLSCs often occupy the upper few hundred meters in the planetary boundary layer (PBL), ~~and their persistent appearance can be persistent relies on when they are associated with a high-pressure system that normally brings a stable PBL that is normally associated with a large-scale subsidence above because of a high-pressure system.~~ These clouds are often formed over cooler subtropical and mid-latitude oceans, constantly covering more than 50% of these areas (Wood, 2012). During the West African monsoon season, LLSCs ~~frequently can also~~ form frequently over continental southern West Africa (SWA) in the night, ~~then and~~ usually break up in the early afternoon of the following day (Schrage and Fink, 2012; Schuster *et al.*, 2013). Under a polluted condition, LLSCs are characterized by numerous and small cloud droplets, increasing the cloud albedo, suppressing drizzle, and extending the cloud lifetime (Twomey, 1957; Haywood and Boucher, 2000; Liu *et al.*, 2014; Carslaw *et al.*, 2017). The presence of LLSCs impacts on the radiative budget of the atmosphere, surface fluxes, the diurnal cycle of the convective boundary layer, and thus the regional climate (Knippertz *et al.*, 2011; Hannak *et al.*, 2017). However, the processes behind the life cycle of LLSCs particularly over SWA remain elusive, the diurnal cycle of LLSCs hence the representation of these clouds is still poorly represented in weather and climate models; especially over is still poor SWA, because the processes behind the variability of LLSCs cover remain elusive (Knippertz *et al.*, 2011; Hannak *et al.*, 2017; Hill *et al.*, 2018).

60 Stratiform clouds are sensitive to aerosol concentration, chemical composition, and vertical distribution. This is because that aerosol can directly scatter or absorb solar radiation (the direct effect or aerosol-radiation effect), or by serving as cloud nuclei, influence cloud microphysical structure and thus reflectance or lifetime (the indirect aerosol effects or radiative effect of aerosol-cloud interaction plus cloud adjustment) (Boucher *et al.*, 2013). ~~The Specifically, the~~ heating associated with aerosol absorption of solar radiation would be able to perturb ~~atmospheric the~~ thermodynamic stability and thus dynamical processes in the atmosphere as well (the semi-direct effect) (Hansen *et al.*, 1998), ~~and Such a semi-direct effect can beserve as a~~ positive or negative addition to the indirect effect depending on the relative distribution of the aerosol with respect to clouds (*e.g.*, Johnson *et al.*, 2004; Feingold *et al.*, 2005). All these effects can modify the energy budget and thus the status of the planetary boundary layer where the stratiform clouds form and evolve. Aerosols inside stratiform clouds can also be modified by aqueous physio-chemical processes, further altering the forcing strength of aerosol population, whether remaining inside droplets or being released through evaporation, due to their modified morphology and chemical composition (Wood, 2012). Interactions between aerosols and clouds, and their effects on radiation, precipitation, and regional circulations, remain one of the largest uncertainties in understanding and projecting climate change. Indeed, the indirect effect of aerosol is still difficult to estimate (Boucher *et al.*, 2013), making any effort to minimize the associated uncertain in the climate models demanding. Climate models struggle to minimize such uncertainties. (Li *et al.*, 2022). Several previous studies were conducted to investigate aerosol-clouds interactions in LLSCs using high-resolution Large-Eddy Simulation (LES) models, though mainly on cases over ocean (*e.g.*, Ackerman *et al.*, 2004; Sandu *et al.*,

80 2008; Twohy *et al.*, 2013; Flossmann and Wobrock, 2019), where surface fluxes often have insignificant diurnal variation and latent heat alongside moisture from evaporation at sea surface dominate, differing from the cases over land (Wood, 2012; Ghonima *et al.*, 2014).

85 During the West Africa Monsoon (WAM), aerosols can come from both local and remote sources to SWA. A large amount of Biomass Burning Aerosols (BBA) can be transported from southern and ~~Central~~ central African towards SWA during the summer monsoon (Haslett *et al.*, 2019). These ~~air masses~~ transporting BBA are also loaded with additional aerosols from anthropogenic emissions upon reaching the highly urbanized regions near the coast (Chatfield *et al.*, 1998; Sauvage *et al.*, 2005; Mari *et al.*, 2008; Murphy *et al.*, 2010; Reeves *et al.*, 2010; Menut *et al.*, 2018; Haslett *et al.*, 2019). A significant quantity of ~~wind-blown~~ mineral dust aerosols emitted from the Sahara and Sahel throughout the year with a peak in springtime (Marticorena and Bergametti, 1996) can also reach SWA, often in June (Knippertz *et al.*, 2017). Local aerosol sources ~~of aerosols~~ in SWA are related to anthropogenic activities near the coast (projected to increase with growing population, Lioussé *et al.*, 2014), from where polluted plumes would transport inland (Deroubaix *et al.*, 2019). ~~These emissions are projected to increase with the expected growth of the population (Lioussé *et al.*, 2014).~~ Different ~~These different~~ emission sources ~~also~~ lead to a 95 complex mix of aerosol constituents in the aera, having a serious impact on human health (Bauer *et al.*, 2019), and possibly complicating the aerosol impacts on the ~~diurnal-life~~ cycle of LLSCs as well as precipitation over SWA (Taylor *et al.*, 2019).



100 **Figure 1.** Map of southern West Africa with Savè, Kumasi and Ile-Ife locations and the flight track (blue line) of the ATR-42 the 3 July 2016 with NASA Suomi NPP/VIIRS true color corrected reflectance (<https://worldview.earthdata.nasa.gov/>).

The DACCIWA project was designed to better characterize cloud-aerosol-precipitation interactions in SWA (Knippertz *et al.*, 2015). The measurement campaign conducted in June-July 2016 has provided a comprehensive set of ground-based and airborne measurements of clouds and aerosols (Knippertz *et al.*, 2017; Kalthoff *et al.*, 2018; Flamant *et al.*, 2018) ~~and inspired model analyses~~. The measurements were conducted at three supersites, Savè (Benin), Kumasi (Ghana) and Ile-Ife (Nigeria) (Fig. 1) and coordinated with three research aircrafts: the French ATR-42 operated by SAFIRE (Service des Avions Français Instrumentés pour la Recherche en Environnement), the British Twin Otter operated by British Antarctic Survey, and the German Falcon aircraft operated by DLR (Deutsches Zentrum für Luft und Raumfahrt). Additional radiosoundings were launched from Savè with high temporal frequency, which specifically benefits the monitoring of the LLSCs ~~diurnal~~ evolution.

115 DACCIWA campaign has also inspired many modeling studies. Based on the observations from DACCIWA and a parcel model, Taylor *et al.* (2019) and Denjean *et al.* (2020a) showed that most cloud condensation nuclei and absorbing aerosols observed during DACCIWA campaign were from ubiquitous long-range transported BBA, causing a polluted background which limits the effect of local pollution on cloud properties and aerosol radiative effects. Using COSMO-ART model in a simulation ~~for~~ of 2-3 July

2016 case, Deetz *et al.* (2018) found that under the influence of the cold air brought by the Maritime Inflow (MI, ~~cold air~~) from Guinean Gulf, stratus-stratocumulus transition is susceptible to the aerosol direct effect, resulting in a spatial shift in the MI front and a temporal shift of the cloud transition. ~~Over SWA and influenced~~ Influenced by anthropogenic emission sources, the break-up time of LLSCs ~~over SWA~~ can be delayed by one hour and daily precipitation rate can decrease by 7.5% according to Deroubaix *et al.* (2022). Moreover, the joint rather than separate impact of the semi-direct and indirect effects of aerosol were also studied ~~together by with~~ varying ~~respective~~ magnitude ~~or emissions~~ of anthropogenic aerosol ~~emissions, though not being examined separately. by~~ Haslett *et al.* (2019) using COSMO-ART model. The study indicated that cloud droplets number concentration could increase up to 27 % due to transported BBA ~~using COSMO-ART~~, making cloud and rain less sensitive to further increase in regional anthropogenic emissions. The impact of sedimentation on LLSCs ~~has been was indicated by previous studies (e.g., Bretherton et al., 2007). This issue has also been addressed in a modeling of DACCIWA case by studied by~~ Dearden *et al.* (2018) using the Met Office NERC Cloud model (MONC), who demonstrated that sedimentation of cloud droplets, determined by droplet size, could affect liquid water path by removing droplets from the entrainment zone, or by lowering the cloud base and creating more heterogeneous cloud structure. Menut *et al.* (2019) showed with-in a WRF-CHIMERE simulation that a decrease of anthropogenic emissions along the SWA coast ~~led could lead~~ to a northward shift of the monsoonal precipitation and ~~the an~~ increase of surface wind speed over arid region in the Sahel, resulting in an increase of mineral dust emission. ~~These previous modeling studies all highlighted in a regional scale while considering only limited aerosol chemical compositions rather than all aerosol species particularly black carbon (BC) measured during the field campaign. Pedruzo-Bagazgoitia et al. (2020) analyzed the stratocumulus-cumulus transition at a fine scale (a dozen of kilometer sidelong) using a LES at high resolution (50x50 m²), though aerosol effects were not being taken into consideration. These previous modeling studies all highlighted in a regional scale. Majority of them did not well use the enrich information of aerosol chemical compositions (e.g., black carbon, or BC) obtained during the field campaign.~~

The aim of this study is to improve our understanding of the ~~specific~~ impacts ~~of associated with both~~ local and transported aerosols on the life cycle of LLSCs during the monsoon period over SWA. In doing so, observational data obtained from the well-documented DACCIWA field campaign have been used to constrain a high-resolution LES model ~~including incorporated with~~ an interactive aerosol module that is able to represent the complex aerosol compositions besides size distributions. This modeling effort is also among a few studies that model and analyze stratiform cloud ~~nocturnal-diurnal~~ life cycle over land rather than ocean. A description of observations, data, and the model as well as configurations of different simulations ~~will be is~~ presented in the Method section after the Introduction. Then the results of an analysis aiming to understand and ~~validate evaluate~~ the modeled reference case against measurements ~~will be are~~ discussed. Thereafter, the results from several sensitivity simulations ~~will be are~~ presented. These sensitivity simulations use various observed aerosol profiles with different size distributions and chemical ~~compositions, compositions and are~~ designed to examine the indirect and semi-direct effects of aerosols on the life cycle of modeled LLSCs. ~~This makes, making these analysis study~~ the first such modeling attempt within the framework of DACCIWA campaign. The last section of the paper ~~will summarize~~s major research findings of this study.

2. Methods

2.1 Observational data

We have used certain measurements of ~~the~~-DACCIWA field campaign ~~to select our LLSC case and~~ to configure the model simulations ~~our LLSC case~~. These data are described as follows.

i) Radiosonde data: During DACCIWA campaign, radiosondes were launched with the MODEM system every 1 to 1.5 hour between 17:00 and 11:00 UTC (the local time of Benin is UTC+1) at the supersite of Savè in Benin. This site is located 185 km from the coast and 166 m above sea level. The area is rather flat, and the vegetation is mainly composed of small trees and shrubs. ~~Vertical profiles from ground to 1500 m altitude Temperature of temperature~~, pressure, relative humidity, and wind ~~vertical profiles were measured with a 1s temporal interval (4 - 5m of vertical resolution) below 1500 m above ground level were measured with a 1s temporal interval (4-5m of vertical resolution)~~ (Derrien *et al.*, 2016). These sondes were obtained using two balloons of different volumes to reach a preset time of ascent, and after the cutting of the larger balloon, the second one would be used to retrieve the sonde for another use (Legain *et al.*, 2013).

ii) Ground-based measurements: At the supersite of Savè, a CHM15k Ceilometer was deployed by the Karlsruhe Institut für Technologie (KIT) to measure the cloud base height continuously with a 1 min interval and a 15 m vertical resolution, based on the backscatter profiles produced by the lidar with a wavelength of 1064 nm and a 5-7 kHz rate (Handwerker *et al.*, 2016). The cloud cover was monitored every day by using a MOBOTIX S15 cloud camera, installed by Université Paul Sabatier (UPS) team, to obtain pictures in visible and IR every 2 min. The aperture angles for the IR channel corresponds to a 158 m x 114 m area at a height of 200 m and ~~the~~ pictures are coded in RGB components. A microwave radiometer (~~the~~ humidity and temperature profiler HATPRO-G4 from Radiometer Physics GmbH) was installed by KIT to measure ~~the~~ brightness temperature to retrieve absolute humidity, liquid water path, and air temperature. The surface heat and radiation fluxes were measured with an energy balance station deployed over grass and bushes. Additional measurements include soil heat flux, air density, and turbulence parameters.

iii) Airborne measurements: The aircraft campaign took place from 29 June to 16 July 2016, conducted collaboratively by three research aircrafts (~~see Introduction~~). In this study, only data from the ATR-42 were used as it flew around Savè between 10:00 and 11:00 UTC and probed the cloud layer. The cloud droplet size distribution was measured with a cloud droplet probe (CDP) (Taylor *et al.*, 2019). The chemical composition for non-refractive compounds was measured with the Aerodyne compact Time-of-Flight Aerosol Mass Spectrometer (HR-ToF-AMS) (Brito *et al.*, 2018). The black carbon (BC) mass concentration was measured with a single particle soot photometer (SP2) (Denjean *et al.*, 2020b). The aerosol size distribution was measured with a custom-built scanning mobility sizer spectrometer (SMPS, 20–485 nm), an ultra-high sensitivity aerosol spectrometer (UHSAS, 0.04–1 μm), and an optical particle counter (OPC GRIMM model 1.109, 0.3–32 μm) corrected for the complex refractive index provided in Denjean *et al.* (2020a). The total number concentration of particles larger than 10 nm was measured by a condensation particle counter (CPC, model MARIE). Meteorological variables such as temperature, humidity, pressure, and wind speed and direction were also measured by

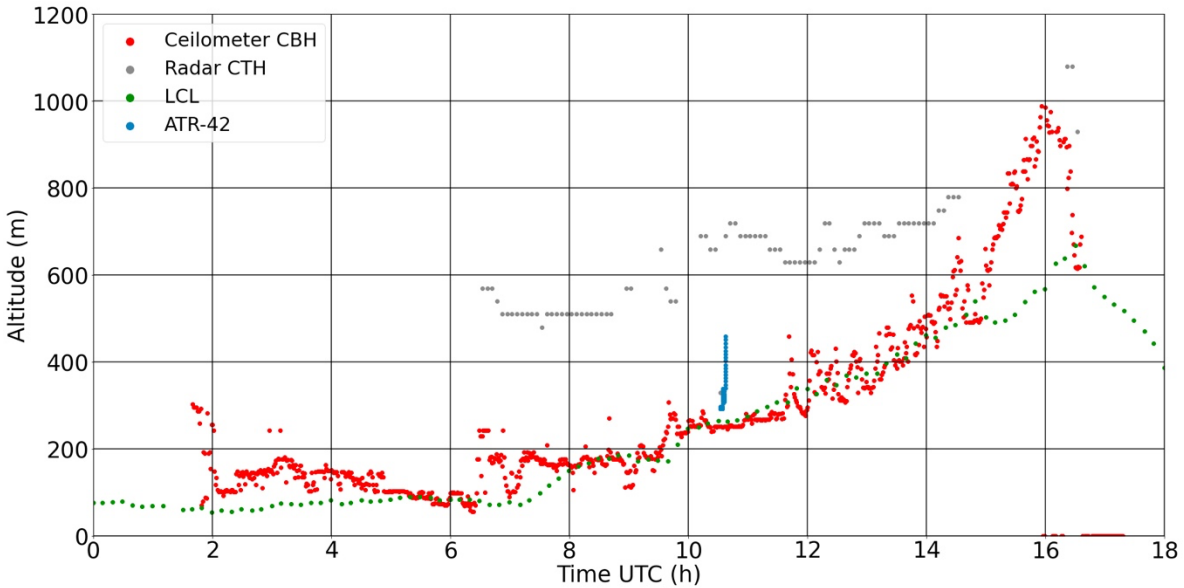
a suite of airborne instruments. A gas concentration analyzer was used to measure certain chemical gases including CO₂, CH₄, and CO.

200

2.2 Description of the studied case

Our study analyzes the ~~diurnal-life~~ cycle of LLSCs based on the observed case of 3 July 2016 at the Savè supersite (Fig. 2). The cloud deck formed during the night, at around 02:00 UTC, close to the appearance of the core Nocturnal-Low-Level Jet (NLLJ), which could have a maximum speed around 6 m s⁻¹ (Kalthoff *et al.*, 2018), associated with a maximum cooling (Lohou *et al.*, 2020). At formation, the cloud ~~had its~~ base and top ~~heights were~~ located around 310 ± 30 m and 640 ± 100 m, respectively, and ~~were was~~ maintained ~~due to by~~ the cloud top radiative cooling and cold advection (Dione *et al.*, 2019).

205



210

Figure 2. 3 July cloud evolution with the representation of the Cloud Base Height (CBH), the Cloud Top Height (CTH), LCL and ATR-42 flight track near Savè.

215

220

The ~~diurnal-life~~ cycle of LLSCs over SWA typically involves four phases: the stable phase, jet phase, stratus phase, and convective phase (Dione *et al.*, 2019; Lohou *et al.*, 2020). The stable phase begins just after sunset and is characterized by a weak monsoon flow and the cessation of buoyancy-driven turbulence within the PBL, generated by surface heating (Zouzoua *et al.*, 2021). The jet phase corresponds to the settlement of key drivers of cooler air advection. Maritime Inflow (MI), a cold and slightly humid air mass from the Guinean coast, often reaches Savè at the end of the afternoon (between 16:00 UTC and 20:00 UTC), then is followed by the NLLJ formation (Adler *et al.*, 2019). The stratus phase begins with LLSC formation when advective cooling continuously increases the relative humidity (RH) until air reaches saturation between 22:00 and 06:00 UTC. The turbulent mixing beneath the NLLJ alongside a strong radiative cooling at the cloud top leads to the persistence of a thick stratus layer (Schuster *et al.*, 2013; Babic *et al.*, 2019). The LLSCs life cycle ends during the final convective phase, which begins

when the PBL develops vertically due to solar heating at the surface alongside a weak radiative cooling at cloud top (e.g., Ghoniya *et al.*, 2016). By using dataset from Savè supersite, Zouzoua *et al.* (2021) identified three scenarios of evolution depending on the LLSCs coupling to the surface at sunrise. The coupling was assessed by the departure between the Cloud Base Height (CBH) and the Lifting Condensation Level (LCL).

The LLSCs observed on 3 July 2016 follow the four aforementioned phases and evolve by scenario C described by Zouzoua *et al.* (2021) as seen in Figure 2. The cloud is coupled to the surface at sunrise (06:30 UTC), its base rises with growing PBL until break-up occurs in the late afternoon around 16:00 UTC. The cloud deck of July 3 case stands longer (2-3 hours more) ~~compared-comparing~~ to other LLSCs observed during the campaign. The co-located Ka band mobile, dual-polarization Doppler radar (8.5 mm, 35.5 MHz) at Savè supersite detected light drizzle precipitation from higher clouds in a rather short period during the first hours of the convective phase, while no precipitation was detected by the surface rain gauge. Thus, ~~this-the~~ late LLSC break-up could be explained hypothetically by the cooling alongside moistening brought by the evaporation of this light precipitation, which could enhance the liquid water path of the beneath LLSC (Zouzoua *et al.*, 2021). Nevertheless, our focus of this study is on the ~~diurnal~~ life cycle of LLSC as influenced by aerosols alongside planetary boundary layer dynamics rather than examining the above hypothesis, which ~~appeared-to-be~~ is likely related to a process beyond the local scale. Therefore, our model setting is made to specifically eliminate the influence of mid-cloud layer for ~~the-this~~ purpose ~~as-described-later~~.

On 3 July 2016, the ATR-42 flew around Savè supersite and probed the boundary layer around 10:00 UTC. The airborne instruments detected aerosol size distributions with a maximum number concentration around 3500 cm^{-3} mainly in the Aikten mode. The ATR-42 also detected an export of polluted air mass from Lomé (a coast city), which could explain the measured high aerosol concentration in the Aikten mode (Denjean *et al.*, 2020a). The measured aerosol chemical composition was mainly dominated by organics (55.3%), followed by sulfates (24.5%), ammoniac (11.2%), and nitrates (6.2%), while only a small amount of BC mass was detected around Savè (2.8%). However, the measured aerosol size distributions were found to need a correction based on aerosol refractive index to avoid bias. For this purpose, Denjean *et al.* (2020a) provided corrected profiles for various types of aerosol populations measured during the DACCIWA campaign. Our modeling has thus used corrected rather than “raw” measurements.

2.3 Meso-NH Model

In this study, we have simulated the observed case using the Meso-NH model (Lac *et al.*, 2018). Meso-NH is a non-hydrostatic atmospheric research model that has been applied to studies in different scales ranging from synoptic to turbulent. Deployed in a limited area, the model uses advanced numerical techniques like monotonic advection schemes for scalar transport, and fourth order advection scheme for momentum (Jiang and Shu, 1996). Sub-grid turbulence is parametrized using turbulence kinetic energy (TKE) based on Deardorff turbulent mixing length. In this study, a fourth order advection scheme CEN4TH, centered on space and time, is applied with a Runge-Kutta centered 4th order temporal scheme for momentum advection (Lunet ~~yet~~ *et al.*, 2017). Aerosol and chemistry are also well represented. Here,

Meso-NH version 5.4.2 is used and the relevant component modules and parametrizations for this study are described as follows.

265 The aerosol-cloud framework of Meso-NH version used in this study is LIMA (Liquid Ice Multiple Aerosol). LIMA includes a complete two-moment scheme predicting both the mass mixing ratio and the number concentration of aerosol species (Vié *et al.*, 2016), using a superimposition of several aerosol modes, with each mode defined by its chemical composition and size distribution. Aerosols can act as either Cloud Condensation Nuclei (CCN) or Ice Forming Nuclei (IFN). Based on the ICE3-ICE4 ice
270 microphysics schemes (Caniaux *et al.*, 1994; Pinty and Jabouille, 1998; Lascaux *et al.*, 2006) and the two-moment warm microphysical scheme C2R2 (Cohard and Pinty, 2000), LIMA also predicts the number concentration of cloud droplets, raindrops, and pristine ice crystals. For modeling boundary layer cloud in LES mode, a pseudo-prognostic approach for correcting the diagnostically derived supersaturation was developed (Thouren *et al.*, 2012) to limit the droplet concentration production and to better represent
275 cloud-top supersaturation ~~better~~. A variant to C2R2, called KHKO, was developed by Geoffroy *et al.* (2008) for clouds producing drizzle (differentiated from cloud droplet with a radius larger than 25 μm) following Khairoutdinov and Kogan (2000) parametrization. The sedimentation of drizzle is calculated in the scheme. The clouds suitable for KHKO are thin and thus low precipitating warm clouds. The precipitating hydrometeors are drizzle only and their diameter are of the order of several dozens of micrometers. These modifications for KHKO alongside necessary modifications were has been brought
280 inside in the LIMA warm phase framework in order to better represent drizzle in thin and low precipitating warm clouds. Therefore, we have adopted this version of LIMA in our modeling.-

To better represent aerosols, we have used the aerosol module ORILAM (Organic Inorganic Lognormal Aerosols Model) in this study and coupled it with Meso-NH to interconnect the cloud
285 microphysics module with LIMA (Tulet *et al.*, 2005). ORILAM describes the size distribution and ~~the~~ chemical composition of aerosols using two lognormal functions respectively for the Aitken and accumulations mode. These modes are internally mixed. For each of them, the model computes the evolution of the primary species (black carbon and primary organic carbon), three inorganic ions (NO_3^- , NH_4^+ , SO_4^{2-}), and condensed water. ORILAM includes a Secondary Organic Aerosols (SOA) module
290 (Tulet *et al.*, 2006) that is, however, not included in this study. Three moments (the zeroth, third, and sixth) are considered for each mode to compute the evolution of total number, median diameter, and geometric standard deviation. Note that the choice of the 6th moment is numerical since it allows one to calculate the coagulation coefficients explicitly and to facilitate the integration of the aerosol solver. The size distribution can evolve through ~~a particle coagulation process with~~ both intra- and intermodal
295 ~~calculations~~ particle coagulation. It can also evolve through condensation and merging between modes. ORILAM includes the CCN activation scheme of Abdul-Razzak and Ghan (2004) in order to replace the one of LIMA to calculate the number of activated CCN. The use of ORILAM needs to activate the gas phase chemistry scheme of Meso-NH (Tulet *et al.*, 2003; Mari *et al.*, 2004) using the EXQSSA solver. ORILAM has a ~~module~~ module for gas-particle thermodynamic equilibrium (EQSAM for inorganics and
300 MPMPO for organics) that allows the model to calculate the contents of inorganic and organic compositions including water within ~~the aerosols~~ (e.g., Metzger *et al.*, 2002; Griffin *et al.*, 2003). The solver ~~will combines~~ moment 0 (integrated number) and 3 (integrated new volume ~~which integrates~~ resulted from the hygroscopic growth) to calculate the new dimensional distribution (Tulet *et*

al., 2005, 2006). ORILAM directly computes the evolution of aerosol extinction, single scattering albedo (SSA), and asymmetry factors that are coupled online with the radiation scheme of Meso-NH for the 6 short wavelengths from the aerosol chemical composition and size parameters (Aouizerats *et al.*, 2010).

ECMWF radiation module is adopted in this study. Based on the two-stream method, this module calculates the atmospheric heating rate and then net surface radiative forcing. Longwave radiation scheme used is the Rapid Radiation Transfer Model (RRTM; Mlawer *et al.*, 1997), based on the correlated k-distribution method. It integrates 16 bands and 140 g points (Morcrette, 2002). The shortwave scheme uses the photon path distribution method (Fouquart and Bonnel, 1980) in six spectral bands. Fluxes are calculated independently in clear and cloudy portions before being aggregated. The liquid cloud effective radius is computed from the liquid water content and droplet number concentration with the Martin *et al.* (1994) parametrization.

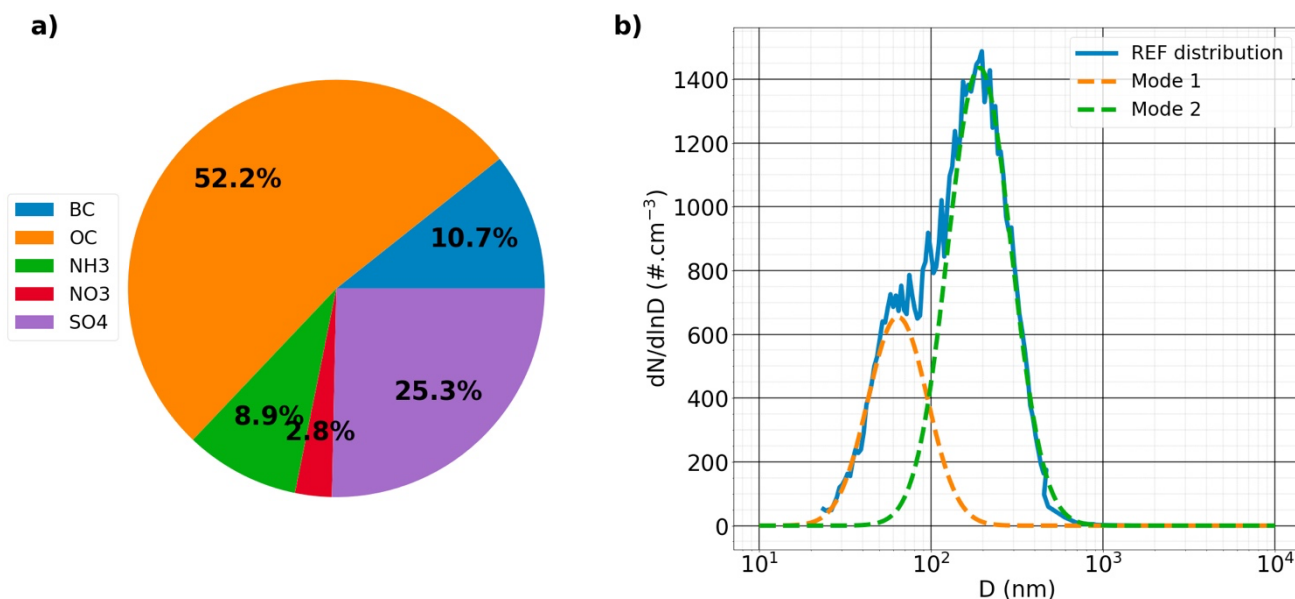
The surface model used in our modeling is the SURFEX, which is a standardized surface module containing surface schemes externalized of Meso-NH (Masson *et al.*, 2013). With SURFEX, each grid point can be split into four tiles: land, town, sea, and inland water (lake, rivers). In case of a shrubs surface, the interactions between soil, biological processes, and the atmosphere are calculated by ISBA parametrization (Noilhan and Planton, 1989). Several evapotranspiration formulations are available for simulating plants and CO₂ fluxes. Soil is represented as a bucket of two or three layers. The land tile can be separated into as many as 19 subtiles following the type of vegetation.

2.4 Model settings

Based on the observations and the capability of the model, a reference case (REF) was first designed to simulate using the LES. The reference case serves as a base for the model to reproduce the major features of the observed LLSCs life cycle particularly using an observed aerosol profile. It also serves as a reference-comparison base for further sensitivity simulations with different aerosol configurations to study the impacts of aerosol composition alongside abundance on LLSCs.

The model domain is a 3D box of 9.6 km x 9.6 km x 2 km in size, with a horizontal resolution of 40 m x 40 m. Note that the radiation module still proceeds its calculations above 2 km using prescribed profiles. The vertical resolution is 10 m between 0 m and 1200 m then 40 m above until 2 km of altitude to explicitly resolve ~~explicitly~~ the important turbulent eddies. A periodic boundary condition on the horizontal directions is applied and ~~an absorbing-“sponge layer”~~ is set between 1.8 and 2 km height to absorb wave reflection. A thermodynamic perturbation is deployed to activate turbulence at the beginning of the simulation at 23:00 UTC of 2 July and the spin-up is 1h (though observed clouds formed around 02:00 UTC). A subsidence profile is applied following Bellon and Stevens (2013) scheme $w_{subs}(z) = -w_0[1 - \exp(-z/z_w)]$, with $w_0 = 15 \text{ mm s}^{-1}$ and $z_w = 250 \text{ m}$. This subsidence profile is applied during the entire simulation to keep a nearly constant cloud top height during the stratus phase and to better control the convective phase. The surface energy and water fluxes are simulated by SURFEX ISBA scheme, parametrized using data from Savè supersite, with the typical vegetation consisting of shrubs, crops, or taller trees, assuming a flat surface in the area around Savè. A time-step of 2s is used, which appears to be adequate based on testing runs to study the LLSCs nocturnal-diurnal variations particularly involving aerosol and cloud microphysics. The radiation scheme is called every 10 minutes. Note that previous studies regarding nocturnal stratus-stratocumulus suggested that a vertical resolution as fine as 5 meters

345 near the cloud top would be necessary for reproducing the cloud top entrainment and thus cloud
 macrophysical structures (Stevens *et al.*, 2005). However, the nocturnal-diurnal life cycle in our case
 involves a dynamically evolving cloud top from 400 to 1200 m, particularly in the daytime, making it a
 difficult task to prescribe a highlighted zone for finer resolution. Our fast-testing results, on the other
 hand, did not suggest ~~an alarming~~ any significant difference between the run with 10 m and 5 m vertical
 350 resolution (not shown). Therefore, the current vertical resolution and the time step are selected to well
 cover all possible cloud tops during the simulation and to provide a best economic computational
 performance for modeling aerosol-cloud interaction with a fully coupled chemistry model.



355 **Figure 3.** Aerosol chemical mass compositions (a) and size distribution fitted into 2 modes described in Table 1 (b) used in
 REF.

| | $N_a (cm^{-3})$ | σ | D (nm) |
|--------|-----------------|----------|--------|
| Mode 1 | 654 | 1.49 | 63.98 |
| Mode 2 | 1530 | 1.53 | 190.97 |

360 **Table 1.** REF aerosol size distribution described by two modes configured by three parameters (number concentration N_a ,
 standard deviation σ and diameter D).

370 REF case is configured using the radiosondes of 2 July at 23:00 UTC for temperature, humidity, and
 horizontal wind components (U, V). The simulation is then ~~controlled-forced~~ by tendency profiles of
 temperature, humidity, and horizontal wind applied homogeneously on the domain each hour. These
 tendency profiles are based on the hourly radiosondes launched on 3 July between 00:00 and 11:00 UTC.
 After 11:00 UTC, the next tendency profiles were ~~designed-derived~~ based on the measurements of the

microwave radiometer, the analysis of surface incoming solar radiative flux, and the cloud thickness and cover. Note that, despite these best possible efforts in configuring a set of observation-constrained
375 tendency profiles to reproduce ~~the~~ observed cloud field, it is difficult to eliminate the possibility that such profiles could reflect certain local thermodynamic effects however small they are. In practice, our main goal is to make the profiles to be able to force the modeled ~~to clouds~~ reproduce observed quantities of major features such as cloud top, base, liquid water path (LWP), surface incoming solar radiation, among others, in the REF case. This would serve the best purpose for us to address the major issue of this study, *i.e.*, the role of different aerosol profiles in the life cycle of modeled LLSCs.

We use a "background" distribution as the aerosol profile for REF simulation. This profile, ~~derived from the corrected original measurements~~ as described in Denjean *et al.* (2020a), reflects the influence of aged BBA on clouds with ~~a~~ minor influence ~~of from~~ local anthropogenic sources. The aerosol ~~number~~ size distribution is dominated by a particle accumulation mode centered at 190 nm and a smaller Aiken mode centered at 64 nm (Figure 3b). This profile exhibits a high loading of aerosols with a maximum of 1400 cm⁻³ ~~detected~~ in the accumulation mode. The aerosol chemical composition is dominated by organics (52.2%), followed by sulfates (25.3%), ammonium (8.9%), BC (10.7%), and nitrates (2.8%). The configuration of ORILAM has been initialized using the REF aerosol chemical composition and size distribution given in Table 1 and Figure 3b by fitting the SMPS profiles into two lognormal modes using
385 the "py-smps" package (Hagan *et al.*, 2022), with each mode having the same chemical composition.

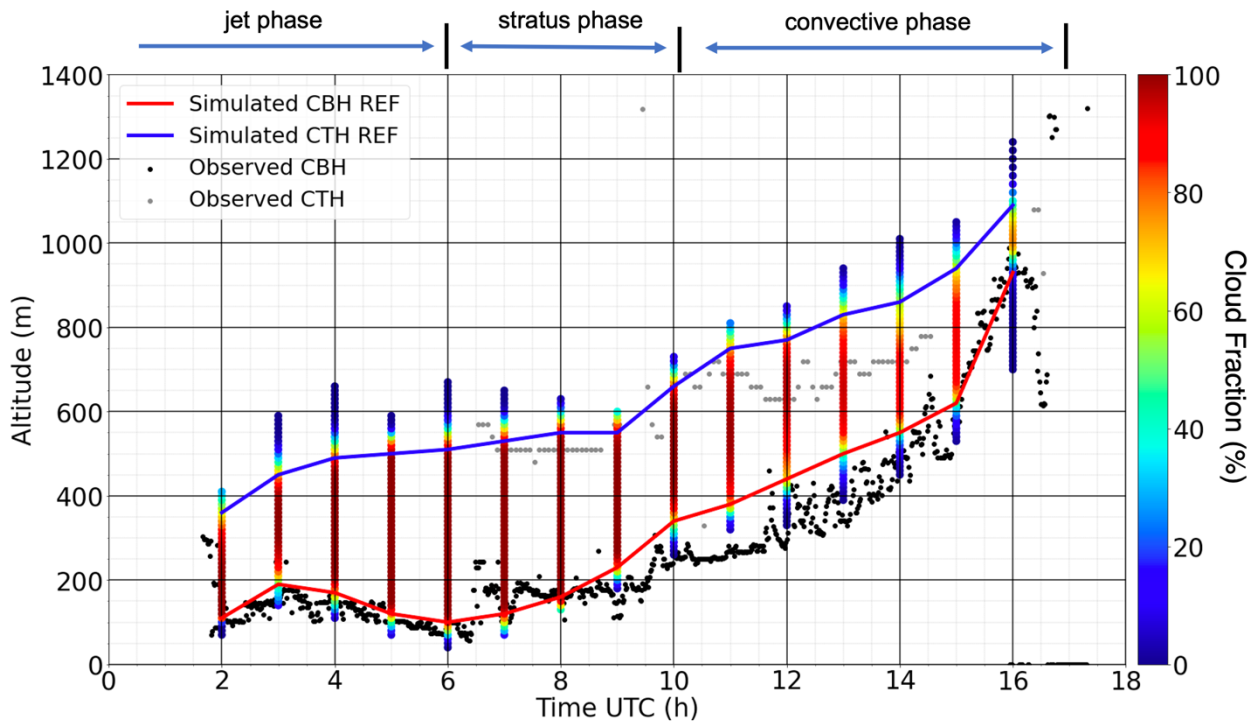
3. Analysis of REF Results

3.1 Simulated ~~the life cycle of~~ LLSCs ~~evolution~~

The simulation of the REF scenario reproduces the formation of the observed LLSCs ~~deck~~ on 3 July
395 2016 as shown in Figure 4. The formation of clouds leads ~~to~~, as described in section 2.2, ~~to~~ the end of the jet phase. The domain mean CBH, ~~estimated~~ ~~derived~~ from the modeled mixing ratio of cloud droplets, follows the ceilometer's measurements during the stratus phase between 02:00 and 10:00 UTC, ~~varies~~ ~~varying~~ between 100 and ~~200-300~~ m of altitude. The simulated ~~domain~~ mean ~~Cloud Top Height (CTH)~~ evolves from 400 to ~~550-650~~ m of altitude ~~during the same period~~, well within the range from 500 to 580
400 m detected by the radar, ~~though during the convective phase, the model result differs slightly from the observations.~~

The modeled ~~domain~~-mean ~~simulated~~ CBH and CTH, ~~however, are~~ overestimated ~~compared to the~~ ~~measurements of~~ ceilometer and radar, ~~respectively, values~~ during some periods in late morning and afternoon. The difference between ~~the~~ simulated and ceilometer detected CBH can be as large as 150 m, ~~e.g., of altitude~~ at 11:00 UTC. While ~~modeled~~ CTH is often ~~overestimated~~ ~~higher than radar~~ ~~measurements~~ by 100 m. Between 15:00 and 16:00 UTC, the simulated ~~mean domain mean~~ CBH approaches again the ceilometer readings (~~from~~ 600 to 950 m) (no radar values are available to ~~validate~~ ~~evaluate~~ the simulated CTH). As mentioned in section 2.1, the ceilometer is a ~~vertically pointing~~ lidar, ~~its~~ ~~while the values detected values are derived come~~ from ~~the reflectivity~~ vertical profiles ~~of reflectivity~~ with
410 a 30 m of resolution. The differences between the model and the observation ~~between 13:00 and 16:00 UTC~~ could come from the different representation ~~of between the~~ simulated result (a domain average) ~~versus and that of~~ ceilometer detection (limited to only ~~one~~ vertical direction), ~~in addition to~~ the vertical resolution of observed profiles, ~~The same could also apply to the difference between modeled and radar~~

415 ~~detected CTH, in addition to~~ the limitation of radar in detecting hydrometeors, ~~and in the end~~ Nevertheless, certain model weaknesses likely associated with a lack of hourly radiosondes during the afternoon period ~~to provide sufficient~~ as an observational constrain ~~would contribute to these discrepancies as well.~~



420 **Figure 4.** Simulated LLSCs deck evolution compared to Savè ceilometer and radar measurements, vertical color bars attribute cloud fraction in percentage at each altitude level. Here simulated CBH and CTH represent domain-averaged cloud base and cloud top height, respectively. Different phases might have overlaps; therefore, their marks only serve a reference purpose here.

425 To analyze the cloud cover profile over the domain, the cloud fraction (CF) at each model layer is calculated as the occupation percentage of all the cloud pixels with a total condensed water mixing ratio exceeding 0.05 g kg^{-1} at each that given model layer (Fig. 4). Note that this cloud fraction differs from the cloud fraction defined as a column metric. In addition, Liquid Water Path (LWP) at each column (Fig. 5), calculated based on column integrated cloud water mixing ratio pixels, brings a view on the horizontal organization and homogeneity of the cloud deck. During the stratus phase, the CF is nearly equal to 100% between CBH and CTH (Fig. 4), suggesting a homogeneous cloud deck consistent with cloud observations with sky camera (visible range) (Fig. 5, the top panels). Notably, peak LWP values between 06:00 and 12:00 UTC are quite close while domain-mean values differ (Fig. 5). In comparison, both peak and domain mean LWP are sharply lower at 16:00 UTC due to cloud break-up and dissipation. Between

435 10:00 and 13:00 UTC, CF of the layers between domain mean CBH and CTH starts to decrease from near
100% to 90%, while CF at CBH and CTH decreases more substantially to reach near 60% and 80%,
respectively. This leads to a less homogeneous cloud deck confirmed by the LWP map and the observation
of the sky camera at 12:00 UTC ~~shown in~~(-the middle row of Figure 5). Indeed, more cloud-free pixels
begin to appear ~~between clouds~~, hence sunlight is seen through the cloud deck by the cloud camera.
440 Finally, CF continues to decrease until the end of the convection phase with a maximum barely reaching
80%, and the values around domain mean CBH and CTH level are as low as 20% and 40%, respectively
(Fig. 4). This demonstrates the break-up of the cloud deck during convection and the cloud thinning. The
bottom panels of Figure 5 clearly show ~~clearly~~ the dissipation of ~~a large number of many~~ cloud blocks
alongside substantially thinning of the ~~others remaining ones~~ at 16:00 UTC.

445

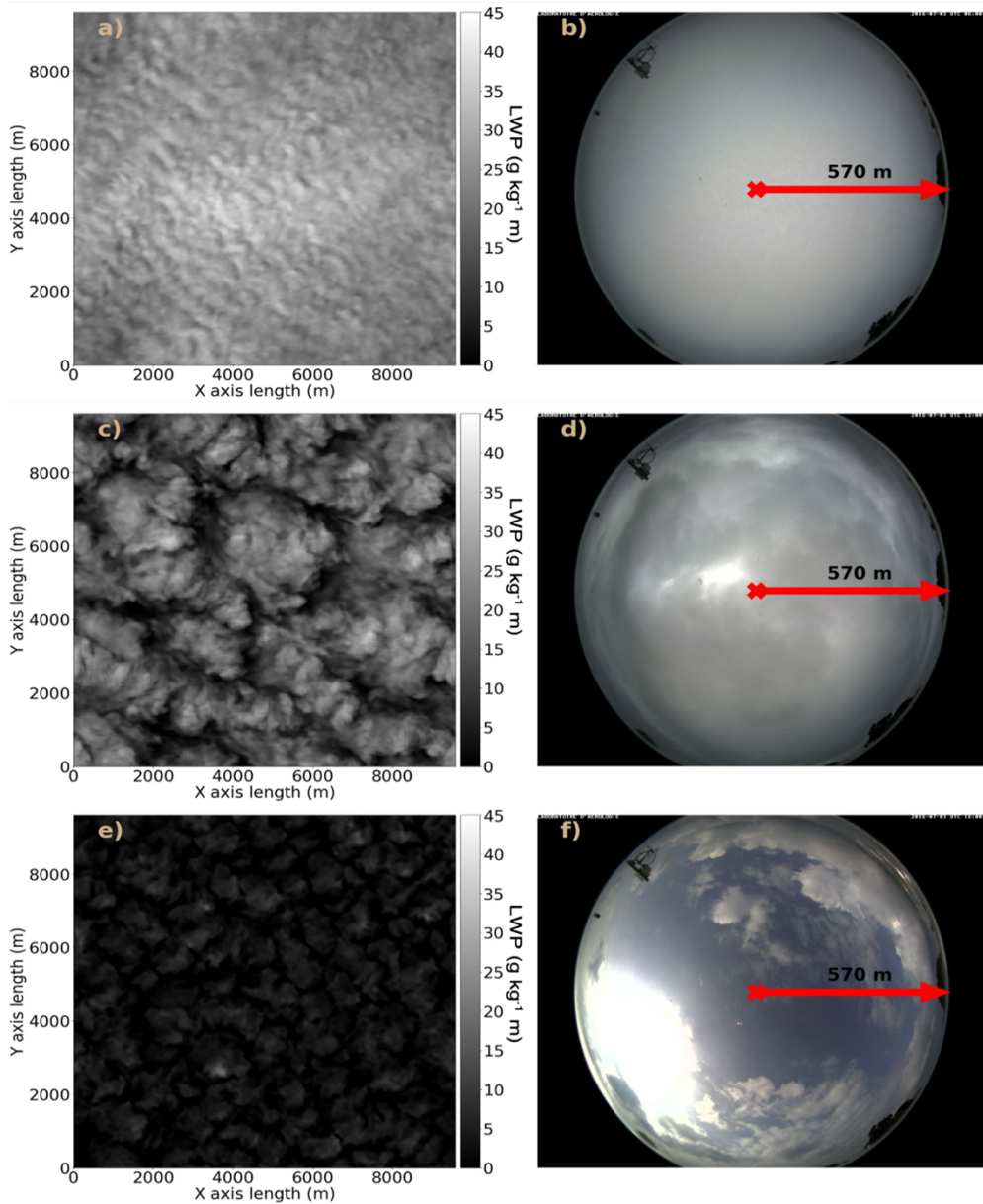


Figure 5. Comparison between modeled liquid water path (LWP, $g\ kg^{-1}\ m$) and the images from Savè cloud camera at 06:00 (top), 12:00 (middle) and 16:00 UTC (bottom).

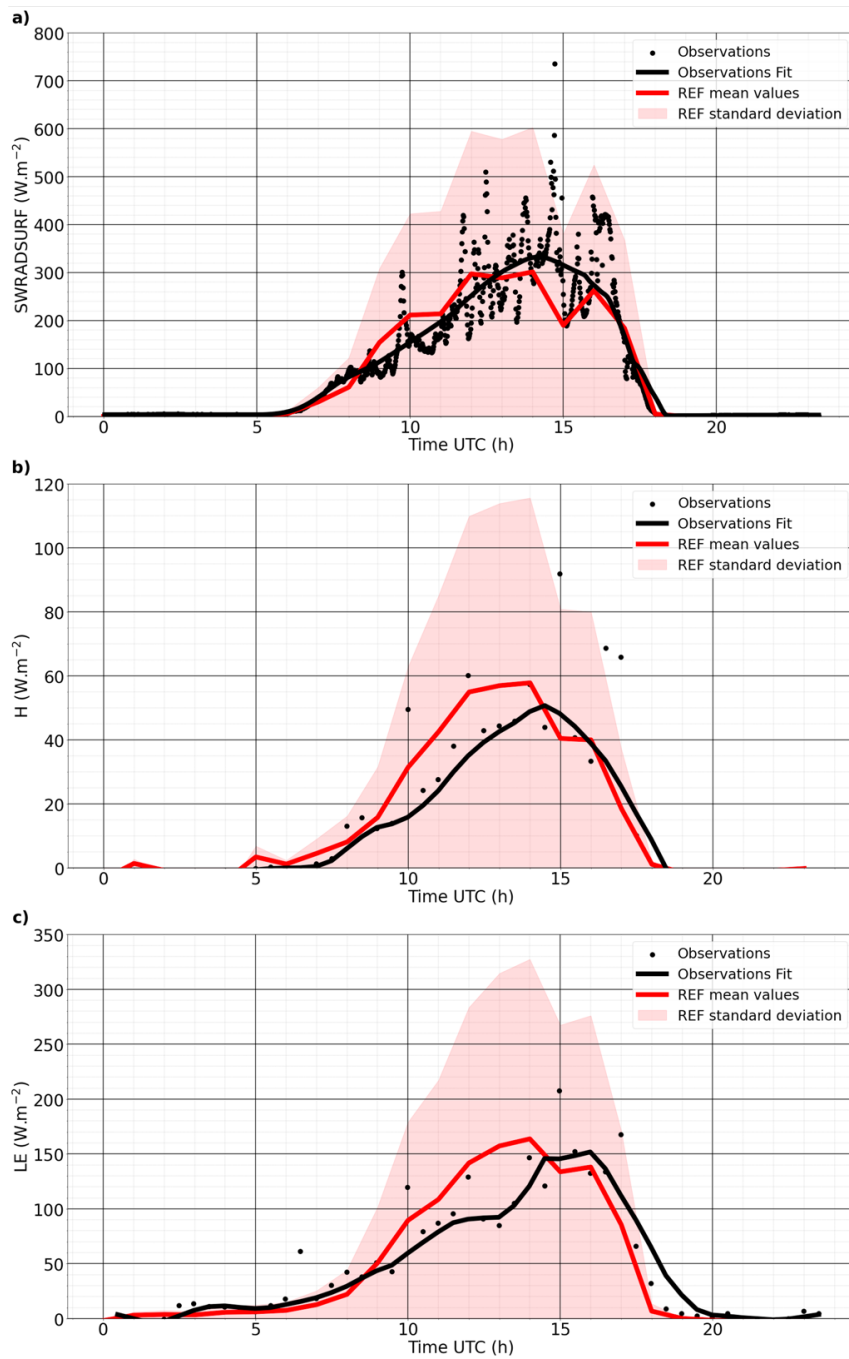


Figure 6. Comparison between Savè surface observation and REF simulation for SW radiation flux at surface (SWRADSURF,a), sensible heat flux (H, b) and latent heat flux (LE, c) all expressed in $W m^{-2}$ at the surface. The variation of REF for each parameter indicates the range of possible values these parameters can take.

Figure 6a shows the comparison between the modeled domain-average shortwave (SW) radiation flux at the surface (SWRADSURF) and the corresponding measurements performed by the energy balance station. Observed values are fitted following the LOcally Weighted Scatterplot Smoothing (LOWESS) method (Cleveland, 1979). The temporal evolution of the modeled SWRADSURF follows the observations rather well despite some biases. ~~After 06:00 UTC, the solar radiation reaches the ground around 06:00 UTC as the cloud deck thickness and covering show little variations. Thereafter, the radiative flux and~~ increases gradually ~~thereafter~~ by reaching near 200 W m^{-2} at the end of the stratus phase (10:00 UTC). As clouds deck becomes inhomogeneous during the convective phase (10:00 to 16:00 UTC), the modeled surface solar flux reaches a maximum of 300 W m^{-2} , which is a bit lower than the fitted 350 W m^{-2} value from measurements. When the clouds break up further, more solar radiation can reach the surface, and model and observation agree well thereafter with an exception at 15:00 UTC, where the mean modeled curve decreases to 200 W m^{-2} while the ~~fitted~~ ~~observati~~oned curve is near 320 W m^{-2} due to an overestimation of the cloud thickness by the model. At 16:00 UTC, both modeled and measurement values are very close around 280 W m^{-2} . Generally, the modeled maximum values are higher than the ones detected by the Savè ground instrument.

Figure 6b and 6c show that the evolutions of the modeled domain-mean latent and sensible heat flux reproduce those measured by the instrument rather well. During the night, the sensible heat flux is negative then increases to 0 W m^{-2} close to the sunrise time (06:00 UTC), indicating a reduction of the cooling close to the ground (Dione *et al.*, 2019). Between 09:00 and 14:00 UTC, the modeled sensible and latent heat flux follow the measured trends though with ~~a clear temporal offset, leading to an overestimate of almost 70 and 18 W m^{-2} , respectively. Then the modeled curves go below the fitted observed curves~~ observations at 15:00 UTC ~~and finally until both merge to almost 0 W m^{-2} after 18:00 UTC. The difference between modeled and observed heat fluxes may be again due to the different representations of area, as modeled quantities are domain-mean values while measurements were made~~ are at a single point.

In Summary, the REF simulation has successfully reproduced ~~all~~ the major observations ~~obtained by the instruments~~ at Savè on 3 July 2016. For example, the modeled cloud thickness and coverage reflect the measured cloud macrophysical status despite some discrepancies, likely due to a lack of hourly radiosonde data to ~~sufficiently correct~~ constrain the tendency profiles ~~to cover the entire simulation period~~ particularly in ~~the~~ afternoon hours. The modeled solar radiation at ground also follows the measurements very well except for certain overestimates. In addition, the sensible and latent heat fluxes measured at Savè have also been well captured by the model ~~despite certain temporal offsets~~.

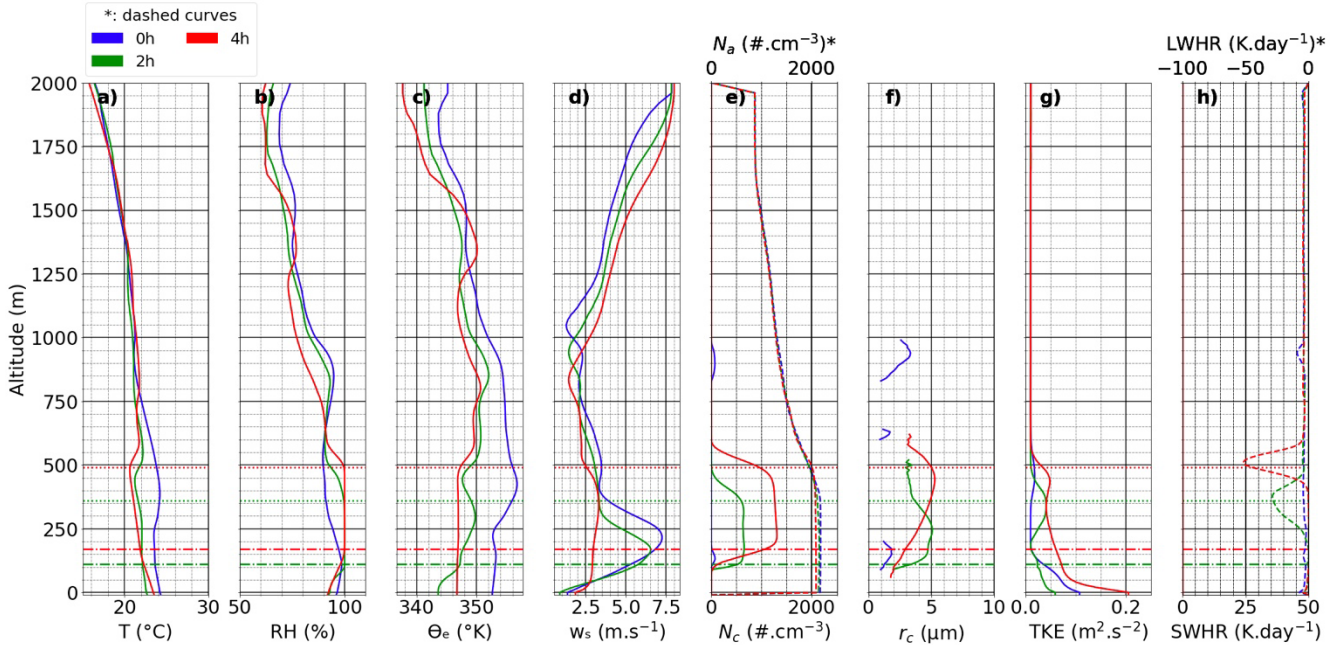
3.2 Thermodynamic, dynamical, cloud microphysical, and radiative analyses

Thermodynamic, dynamical, and radiative processes and their interaction with cloud microphysics are among the key factors in determining the life cycle of LLSCs. Here we discuss the evolutions of these processes simulated by the model in the REF case to better understand the reasons behind model-observation consistency or discrepancy. The discussion will be emphasized on three periods. ~~The first period is:~~ the transition between jet and stratus phase ~~when cloud forms~~ (between 00:00 and 04:00 UTC), ~~to observe the formation of the clouds. The second period is~~ the stratus phase between 06:00 and 10:00 UTC, ~~when the stable cloud layer was observed, by instruments at Savè. The third period is and~~ the

convective phase between 12:00 and 17:00 UTC ~~corresponding to the break-up stage of to study how the properties of LLSCs evolve during the break-up stage.~~

500 3.2.1 Transition jet-status phase

Figure 7 ~~gives-displays the~~ modeled domain-averaged profiles of selected macro- and microphysical features for the transition of jet to status phase, when maritime inflow already reached the site. As expected, the advection of cold and slightly humid air leads to an increase of relative humidity (RH) to reach 100% at 02:00 UTC at 100 m above ground. After this time, RH exceeds saturation between 100 and 500 m of altitude. The inversion occurs around 325 m and 500 m respectively at 02:00 UTC and at 04:00 UTC. The NLLJ is well represented in modeled results as the mean wind speed (w_s) before cloud formation is greater than 7 m s^{-1} . After cloud formation, the NLLJ core nearly corresponds to the mean cloud base height (Adler *et al.*, 2019; Babic *et al.*, 2019; Lohou *et al.*, 2020). The turbulence during this period is shear-driven due to this NLLJ, yielding a well-mixed sub-cloud layer. The turbulent kinetic energy (TKE) is high above ground (0.05 to $0.21 \text{ m}^2 \text{ s}^{-2}$), then decreases to near zero above rough 200 meters at 00:00 UTC. ~~After-At~~ 02:00 and 04:00 UTC, TKE increases at the level of CTH (350 and 500 m, respectively) and decreases at the center of clouds (near zero and $0.04 \text{ m}^2 \text{ s}^{-2}$), indicating this area is less turbulent than the extremities of the cloud layer.



515 **Figure 7.** Profiles from left to right of temperature (T, a), relative humidity (RH, b), equivalent potential temperature (θ_e , c), horizontal wind speed (w_s , d), aerosol number concentration (N_a , dashed curve, e), cloud droplets number concentration (N_c , plain curve, e), mean cloud droplet radius (r_c , f), turbulent kinetic energy (TKE, g), longwave heating rate (LWHR, dashed curve, h) and shortwave heating rate (SWHR, plain curve, h) at 00:00, 02:00 and 04:00 UTC. The horizontal dashed dot lines represent mean cloud base height (CBH) and dotted horizontal lines represent the mean cloud top height (CTH).

520

Cloud droplet number concentration or CDNC (N_c) is determined by the supersaturation in an updraft ~~at cloud base~~ and the ~~concentration number~~ of aerosols that ~~can~~ activate at this supersaturation. In Figure 7e, simulated aerosol concentration is the highest close to the ground then decreases with altitude up to around 2 km. ~~This simulated aerosol profile is,~~ similar to the airborne measurements during DACCIWA (Taylor *et al.*, 2019; Denjean *et al.*, 2020a; Deroubaix *et al.*, 2019; Flamant *et al.*, 2018). The simulated cloud microphysical features reflect a polluted condition as N_c reaches ~~above 1750-1200 droplet cm^{-3}~~ and mean cloud droplet radius r_c around $5 \mu m$ that is not enough to form drizzle (~~larger than $25 \mu m$ as defined in the model; typical size reaching the ground can be~~ between 0.2 mm and 0.5 mm; ~~ref.~~ Pruppacher *et al.*, 1998; Sandu *et al.*, 2008). These ~~modeled~~ values are in the range of corresponding measurements at the same altitude by Taylor *et al.* (2019). ~~The median of simulated CDNC is 500 droplets cm^{-3} at the beginning of cloud formation then reaches 1750 droplets cm^{-3} later, most likely due to the continuous activation of aerosol into cloud droplets.~~

The emission of thermal radiation by the clouds during the stratus phase creates a cooling at the cloud top as demonstrated by the evolution of modeled Long-Wave Heating Rate (LWHR) profiles at Figure 7h. ~~For LLSCs at this stage with many low LWP blocks, The the~~ more numerous the cloud droplets are the stronger the cooling is (*e.g.*, Petters *et al.*, 2012), as shown in Fig. 7h that LWHR can reach $-50 K day^{-1}$. This strong longwave emission can reduce the thermal production of turbulence above the cloud top, deepening the temperature inversion. A stabilized cloud top layer by radiative cooling and a NLLJ core contributing to the shear-driven turbulence below the cloud base leads to a well-mixed cloud layer, making the LCL to correspond to the LLCs base as seen in Figure 2 (Adler *et al.*, 2019; Lohou *et al.*, 2020).

3.2.2 Stratus phase

The stratus phase starts just after the sunrise. Maintaining stratus in almost the same state throughout this phase needs ~~a certain proper stable ground~~ temperature and ~~moisture supply humidity conditions~~. As shows in (Figure 8), between 06:00 and 08:00 UTC the ground temperature varies little around $23^\circ C$, supersaturation still exists between CBH and CTH, and air masses are quite well-mixed within ~~the boundary layer~~ as θ_e is near constantly at 347 K (~~Fig. 8c) throughout the boundary layer and the inversion layer is settled where θ_e is reaching 350-351 K~~). The horizontal wind speed between the ground and the cloud base decreases ~~from the magnitude in the previous transition phase (Fig. 8d), which indicates indicating~~ a weakening NLLJ core (nearly $2 m s^{-1}$); ~~then rises with altitude due to the turbulent mixing induced by the LW cooling at the cloud top during the night. The turbulence TKE value~~ between ground and cloud center decreases ~~from its previous magnitude~~ to $0.03 m^2 s^{-2}$; ~~then finally increases while increases~~ slightly to $0.04 m^2 s^{-2}$ at the mean CTH. ~~The TKE is a bit stronger a~~ At 08:00 UTC, TKE reaches ~~ing~~ $0.05 m^2 s^{-2}$ in the cloud layer, ~~implying owing to~~ an increase of surface solar heating (Fig. 8g).

The aerosol concentration ~~at from~~ 06:00 and 08:00 UTC is around $2000 cm^{-3}$ ~~up to below~~ 500 m altitude, then decreases along altitude. ~~This concentration which~~ is high enough to sustain a CDNC of 1100-1200 ~~droplets cm^{-3}~~ between CBH and CTH ~~as shown in Fig. 8e~~. The ~~concentration of cloud droplets leads to a~~ maximum layer-mean droplet radius ~~of is about~~ $6 \mu m$, ~~which is~~ still not enough to form ~~a significant~~ drizzle. The cloud layer has an albedo close to 1 due to the high CDNC. The presence of light absorbing aerosol amplifies the Short-Wave Heating Rate (SWHR) at the cloud top ~~by semi-direct effect~~.

At 08:00 UTC, the maximum SWHR and LWHR are about equal to 27-25 $K day^{-1}$ and -6070 $K day^{-1}$, respectively (Fig. 8h).

At 10:00 UTC, the cloud layer starts to rise significantly, with CBH and CTH reaching 340 and 660 m, respectively (Fig. 8). Moreover, stronger solar irradiance reaches the ground ($220 W m^{-2}$), leading to the heating of the surface and the increasing of the sensible and latent heat fluxes as seen in Figure 6. It also increases the surface temperature near ground to $24 ^\circ C$ and at the cloud top to $20 ^\circ C$ (Fig. 8a). ~~The inversion layer is observed above the cloud top between 660 and 750 m.~~ The NLLJ core is no longer present at this moment. TKE increases to $0.1 m^2 s^{-2}$ throughout the vertical layer from 50 meter above the ground to a level just below the cloud top (Fig. 8g). This enhancement of turbulence is expected to increase entrainment entering the cloud from above as well. The SWHR increases to $45 K day^{-1}$, almost compensates the LWHR cooling of $625 K day^{-1}$.

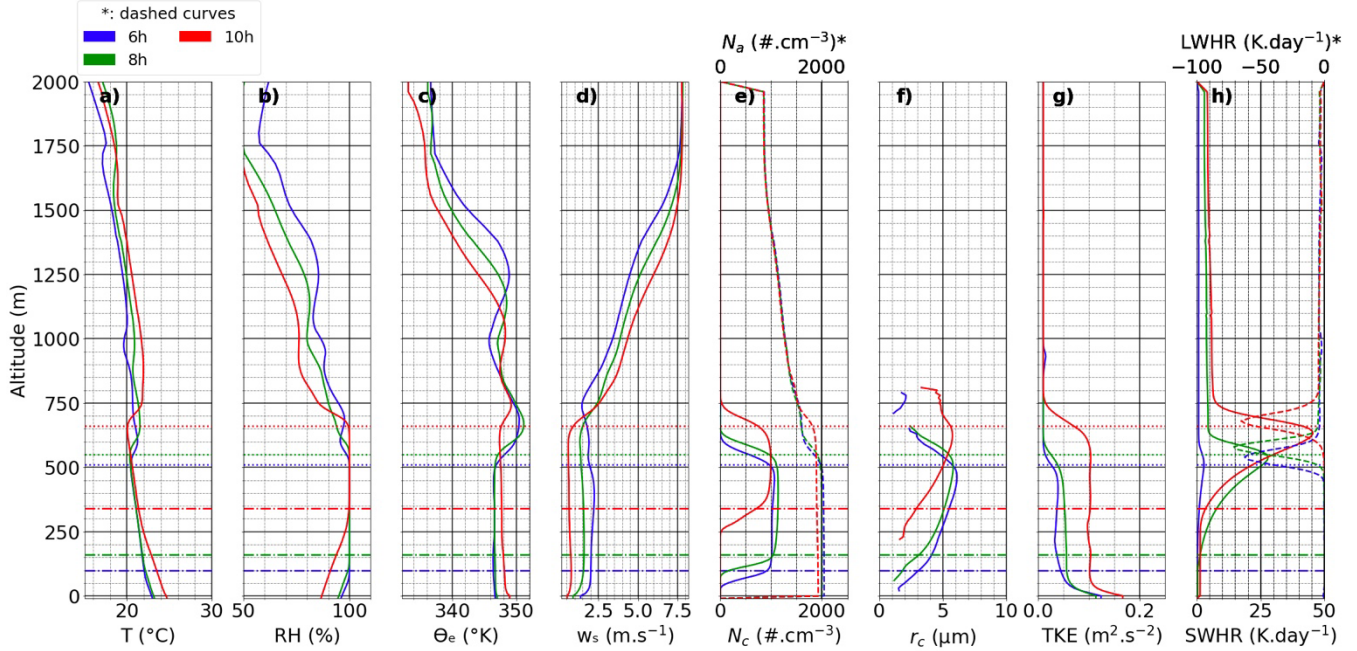


Figure 8. Profiles from left to right of temperature (T, a), relative humidity (RH, b), equivalent potential temperature (θ_e , c), horizontal wind speed (w_s , d), aerosol number concentration (N_a , dashed curve, e), cloud droplets number concentration (N_c , plain curve, e), cloud droplet radius (r_c , f), turbulent kinetic energy (TKE, g), longwave heating rate (LWHR, dashed curve, h) and shortwave heating rate (SWHR, plain curve, h) at 06:00, 08:00 and 10:00 UTC. Dashdot horizontal lines represent mean cloud base height (CBH) and dotted horizontal lines the mean cloud top height (CTH).

580 3.2.3 Convective phase

This phase extends from 12:00 to 17:00 UTC on 3 July 2016. During this period, surface SW radiation flux is maximized at $300 W m^{-2}$ (Figure 6), leading to an intense the highest surface heating of the day. As a result, and an increase of the ground temperature evolves from 25 to $27 ^\circ C$ as seen at (Figure Fig. 9a). Convection of humid air masses causes the CBH and CTH to rise from 450 to 925 m and from 760 to 1100 m, respectively. ~~The formation of clouds is still possible due to RH exceeding 100% in upper altitude.~~ Moreover, at 16:00 UTC, the equivalent potential temperature decreases above 450 m of altitude,

indicating ~~an unstable~~ air masses ~~become more unstable with altitude~~ there. The horizontal wind speed is weak at the beginning of the phase with 0.5 m s^{-1} at ground level but increases along time to reach 1 m s^{-1} ~~at ground~~ and ~~from 1 to 3~~ m s^{-1} around 700m ~~altitude~~. This increase coincides the dissipation of the LLSCs and indicates the arrival of the marine inflow.

The turbulence profiles TKE value below the cloud base evolve along altitude during the convection phase is higher or similar to that inside the cloud from 12:00 to 14:00 UTC, reaching $0.075 \text{ m}^2 \text{ s}^{-2}$ in center of clouds and almost zero near 850 m at 12:00 UTC showing a well-mixed PBL (Fig. 9g). By 14:00 UTC, TKE reaches $0.25 \text{ m}^2 \text{ s}^{-2}$ inside the cloud, indicating a reinforcement of turbulence. At From 16:00 UTC, TKE decreases near the ground but increases at cloud level to a value of $1.50.15 \text{ m}^2 \text{ s}^{-2}$, showing a strong turbulence layer ~~therewithin the vertically lifted while thinner cloud due to enhanced convection~~. This layer further moves to an upper altitude after 17:00 UTC.

The aerosol distribution varies along with the dynamical situation. ~~The, with a~~ maximum aerosols concentration reaches ~~reaching~~ $1800\text{-}1700 \text{ cm}^{-3}$ below 800 m at 12:00 and 1700 cm^{-3} below 1000 m at 17:00 UTC within the PBL. As a result, ~~t~~ The domain mean CDNC has a maximum value of 900 droplets cm^{-3} at 12:00 UTC. This value ~~then~~ decreases along time as more clouds dissipate (Fig. 9e). After clouds ~~become thinner and~~ start to break ~~and become thinner~~, reduced cloud coverage CF allows more solar radiation to reach the ground. The maximum value of SWHR ~~drastically~~ changes from 45 K day^{-1} at 12:00 UTC (almost compensating ~~the longwave cooling at cloud top~~ cooling) to about 10 K day^{-1} at 16:00 UTC. The cloud top LW cooling is near constant at the end of convection phase with -45 K day^{-1} (Fig. 9h).

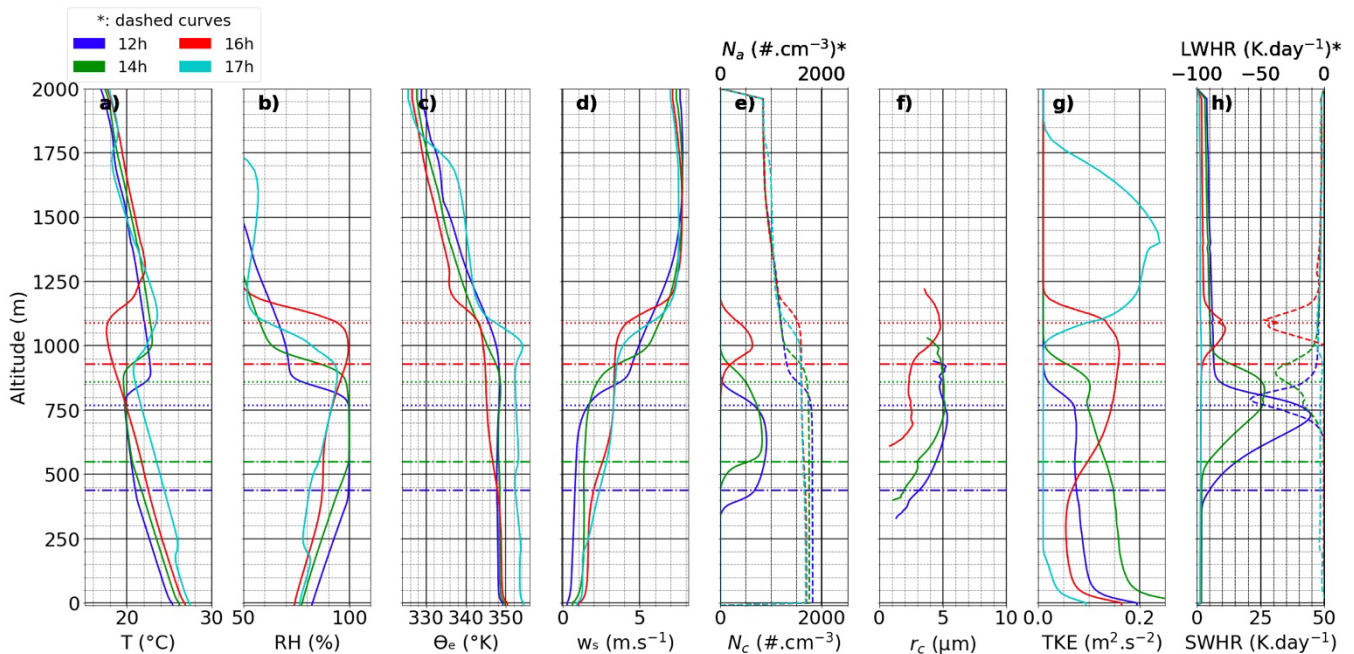


Figure 9. Profiles from left to right of temperature (T, a), relative humidity (RH, b), equivalent potential temperature (θ_e , c), horizontal wind speed (w_s , d), aerosol number concentration (N_a , dashed curve, e), cloud droplets number concentration (N_c , plain curve, e), cloud droplet radius (r_c , f), turbulent kinetic energy (TKE, g), longwave heating rate (LWHR, dashed curve, h).

h) and shortwave heating rate (SWHR, plain curve, h) at 12:00, 14:00, 16:00 and 17:00 UTC. Dash-dot horizontal lines represent mean cloud base height (CBH) and dotted horizontal lines the mean cloud top height (CTH).

4. Sensitivity Study to Examine the Influence of Different Aerosol Profiles on LLSC Life Cycle

615 Previous studies have indicated that the life cycle of stratus or stratocumulus within the planetary boundary layer depends on ~~the a~~ subtle balance among several critical while interconnected forcings, including surface heat fluxes, cloud top and base radiative profiles, and thus turbulent mixing (e.g., Stevens *et al.*, 2005; Dussen *et al.*, 2014, Ghonima *et al.*, 2016). ~~Apparently, o~~ Our simulation results of the REF case support previous findings particularly for the cases over land, ~~wherewith the~~ surface sensible heat playing a significant role. Nevertheless, the role of aerosols in such a life cycle have rarely been examined in depth. Given the critical role of aerosols in determining cloud macro- and microphysical features and thus radiation, this is an important critical issue to address ~~in order to to~~ advance our understanding of the LLSC life cycle. A unique component of our study is the deployment of an interactive aerosol and atmospheric chemistry module in ~~this the~~ observation-constrained LES modeling ~~effort framework~~. The REF simulation has demonstrated that this model is capable to reproduce many observed dynamical, thermodynamic, and aerosol features of the July 3 LLSC case despite certain biases. Thus, we have designed additional sensitivity simulations, and using the results of REF run as a base to further isolate the aerosol impacts on LLSC life cycle through: (1) the difference in cloud droplet number concentrations resulted from aerosol profiles that differ in both number concentration and chemical composition; and (2) the semi-direct effects from absorption of black carbon aerosols. In the following sections, we will discuss the modeling configurations alongside outcomes of these two sets of simulations. likely impacts of aerosol variations in both number concentration and chemical composition on the life cycle of observed LLSCs.

635 4.1 Impact of different aerosol profiles on micro- and macrophysical properties of LLSCs Aerosol profiles used in sensitivity simulations

The result of REF simulation ~~has demonstrated that the Meso-NH model is able to reproduce many observed features of the July 3 LLSC case despite certain biases. Moreover, the dynamical, thermodynamic, and aerosol parameters are reasonably captured by the model. To further reveal the impacts of aerosols from different emission sources on the life cycle and key aerosol-cloud radiation processes of modeled July 3 2023 LLSC case, w~~ We have firstly configured two additional sensitivity simulations with observation-based aerosol scenarios profiles differing from the one used in REF run; ~~based on observations during the field campaign~~ (Figure A1 and Table 2). The first is an experiment with first simulation uses an aerosol profile that reflects an influence of heavy anthropogenic pollution, obtained based on the aerosol chemical composition and size distribution observed by Brito *et al.* (2018) and Denjean *et al.* (2020a) within urban plumes originated from cities of Lomé, Accra and Abidjan, hereafter referred as POL. The second is an experiment a simulation designed using that uses a clean aerosol profile derived by dividing REF aerosol concentration by 10, called CLEAN. then applied them in a set of These two sensitivity simulations ~~that would be~~ otherwise configured the same as the ~~configuration of~~ REF simulation. Comparing to REF case, aerosol profile of POL has a slightly higher peak number concentration but in a different mode. In addition, sulfate mass ratio in POL aerosol profile

is much higher than that of in REF profile, while organic carbon mass ratios are quite close in both profiles. REF, POL, and CLEAN runs simulate the July 3 case with different aerosol number concentrations and chemical compositions as reflected in their size distributions. Therefore, these simulations are expected to produce different CDNCs alongside dynamical consequences. Comparison between their results could provide us with information about the aerosol impacts on LLSC life cycle through abundance.

| Case | | $N_a (cm^{-3})$ | σ | D (nm) |
|-------|--------|-----------------|----------|--------|
| POL | Mode 1 | 17100 | 1.54 | 55.19 |
| | Mode 2 | 2650 | 2.14 | 101.83 |
| CLEAN | Mode 1 | 65 | 1.49 | 63.98 |
| | Mode 2 | 153 | 1.53 | 190.97 |

Table 2. Aerosol size distribution parameters for POL and CLEAN_r runs including number concentration, standard deviation, and diameter r_f for two aerosol modes.

~~To investigate the impacts of anthropogenic and biomass burning sources on cloud life cycle, three additional numerical experiments were performed in addition to REF (Table 2). The first is an experiment with aerosol profile that reflects an influence of heavy anthropogenic pollution, obtained based on the aerosol chemical composition and size distribution observed by Brito *et al.* (2018) and Denjean *et al.* (2020a) within urban plumes originated from cities of Lomé, Accra and Abidjan, hereafter referred as POL. The second is an experiment designed using a clean aerosol profile derived by dividing REF aerosol concentration by 10, called CLEAN. The last one contains three experiments without aerosol semi direct effect for CLEAN, POL, and REF aerosol profiles, respectively, called ADEOFF runs, which form paired simulations correspondingly with original CLEAN, POL, and REF runs, i.e., the ADEON runs of these scenarios.~~

4.2 Impact of aerosol loads on micro and macrophysical properties of LLSCs

Regarding the modeled macrophysical features, the domain mean CBH and CTH and cloud fraction of REF and POL are almost the same until 08:00 UTC (Figure 4 and A2). After sunrise, the mean CBH in POL is about 10 m lower than that in REF, reaching 340 m at 10:00 UTC, while the mean CTH is only 10 m higher at 940 m at 15:00 UTC, indicating a slightly thinner cloud layer in POL than REF. The cloud fractions in both cases are also largely the same until the extensive break-up occurs, when the cloud extent in POL displays an evident difference from that in REF, i.e., 670 m thick (from 630 to 1300 m above the ground) at 16 UTC in POL versus 540 m in REF. On the other hand, Indeed, POL and REF have produced clearly different cloud microphysical features including droplet number concentrations alongside mean radius throughout the lifetime of modeled clouds (Figure 10a and 10b). At the time of cloud formation (02:00 UTC), despite having a similar liquid water content (LWC) around $0.35 g m^{-3}$ at 250 m in both cases, N_c^{POL} reaches 333 droplets cm^{-3} and r_c^{POL} 6.45 μm instead of 653 droplets cm^{-3} and 5.1 μm for REF case, indicating a result of differences mainly in Mode 2 aerosol numbers between the two scenarios

685 (at 02:00 UTC the updraft near cloud base is rather weak at less than 0.30 m s^{-1} in both cases). This trend
is about to reversed at 06:00 UTC when the CDNC and radius are equal to $1208 \text{ droplets cm}^{-3}$ and $6.43 \mu\text{m}$
in POL, and $1305 \text{ droplets cm}^{-3}$ and $6.12 \mu\text{m}$ in REF, respectively. After 08 UTC and until the cloud
break up, N_c^{POL} is superior to much higher than N_c^{REF} by reaching with a maximum difference of 1425
690 droplets cm^{-3} at 14:00 UTC. Their respective radii are $4.42 \mu\text{m}$ and $5.18 \mu\text{m}$ while the liquid water content
profiles are quite the same as near 0.47 g m^{-3} at 750 m. The difference between POL and REF in CDNC
after sunrise suggests that the activation favors the POL profile with higher sulfate content when updraft
is strengthened. These above results of CDNC are in good agreement with the ACPIM parcel model
simulation done by Taylor *et al.* (2019) where CDNC varies in a range of 500–1400 droplets cm^{-3}
depending on the inland or offshore (offshore + local emissions) aerosols origin.

695 The difference between CLEAN and REF in ~~cloud macrophysical features such as CBH and CTH is~~
~~visible though largely limited to a few tens of meters. However, their differences in cloud fraction and~~
microphysical features are rather also significant. As expected, from formation to break-up of the clouds,
 N_c^{CLEAN} is lower than N_c^{REF} and r_c^{CLEAN} is larger than r_c^{REF} . At 02:00 UTC, N_c^{CLEAN} has a maximum value
of $181 \text{ droplets cm}^{-3}$ and r_c^{CLEAN} of $7.58 \mu\text{m}$, in comparison to $653 \text{ droplets cm}^{-3}$ and $5.1 \mu\text{m}$ for N_c^{REF} and
700 r_c^{REF} respectively with the same liquid water content value (0.35 g m^{-3}). r_c^{CLEAN} further increases to 12.55
 μm at 08:00 UTC, then decreases slowly to a maximum value of $10.97 \mu\text{m}$ at 14:00 UTC with LWC^{CLEAN}
reaches near 0.45 g m^{-3} instead of 0.49 g m^{-3} for LWC^{REF} , likely due to an increased activation ratio of
aerosols after sunrise. Despite a relatively larger droplet size in CLEAN than POL and REF case, there is
no clear sign of ~~massive formation of significant~~ drizzles even during the convection stage (Fig. 10).
705 Nevertheless, sedimentation thus evaporation of larger droplets from entrainment zone and cloud base
could likely create a thermodynamic perturbation (e.g., Stevens *et al.*, 1998; Jiang *et al.*, 2002). Consistent
with certain previous findings (e.g., Bretherton *et al.*, 2007), in a LES simulations using passive aerosol
profile for July 4-5 DACCWA case, Dearden *et al.* (2018) found that the sedimentation would remove
droplets from the entrainment zone thus, through a feedback, lead to a cloud deck with higher LWP while
710 smaller CF than the case where sedimentation is completely excluded. This could imply a similar contrast
between CLEAN and the two polluted cases in our simulations, by simply assuming the total drizzle
sedimentation amount is proportional to the droplet size (*i.e.*, inversely to the CDNC), though the quantity
of such a perturbation seems rather small here, not to mention the more sophisticated feedback involved
in our case introduced by the dynamic aerosol-cloud interaction in our model.

715 As demonstrated from above discussions that modeled cloud microphysical features generally
respond to the variation of aerosol number concentration as expected, *i.e.*, higher aerosol concentration
leads to higher cloud droplet number concentration (POL > REF > CLEAN) while smaller mean droplet
radius (POL < REF < CLEAN) and hence a higher cloud reflectivity (POL > REF > CLEAN). Though
exception does exist. For example, differences in the aerosol size distribution and chemical composition
720 between REF and POL could lead to an outcome opposite to the general expectation particularly under a
weak dynamical condition updraft. As shown in Fig. 10c, the response of the incoming solar radiation at
ground (SWRADSURF) does not always follow such an expectation in cloud microphysics and thus
reflectivity in responding to aerosol variation. In fact, SWRADSURF appears to be higher in POL than
REF from sunrise to 13:00 UTC, and the values in both runs are also clearly higher than that in CLEAN.
725 This tendency is only reversed after 13:00 UTC when solar flux reaches its peak until the break-up stage.

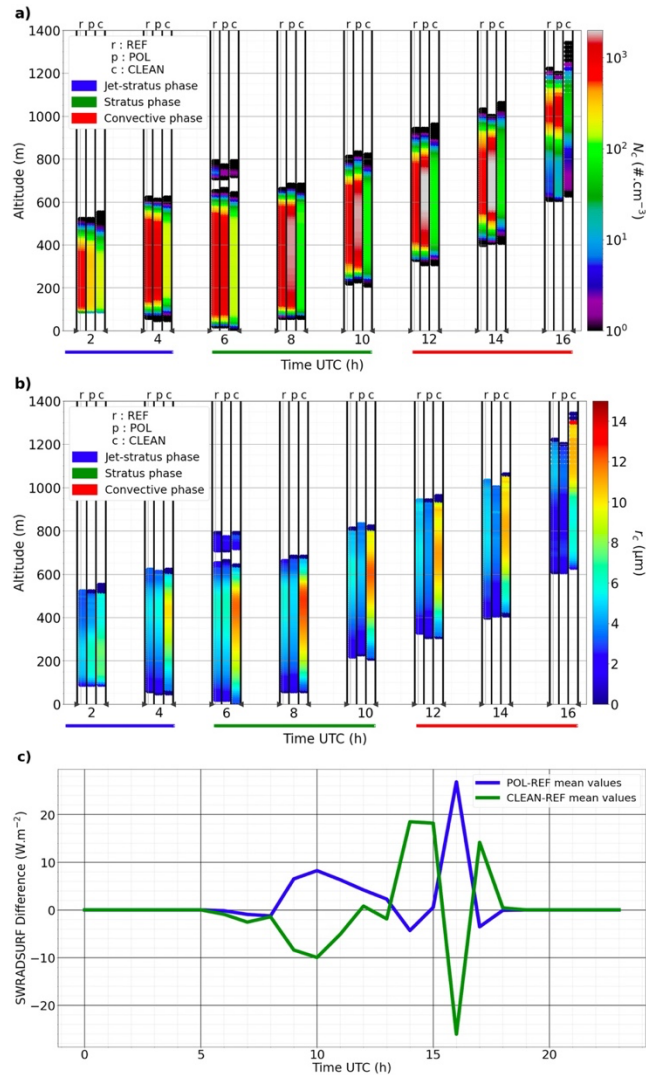
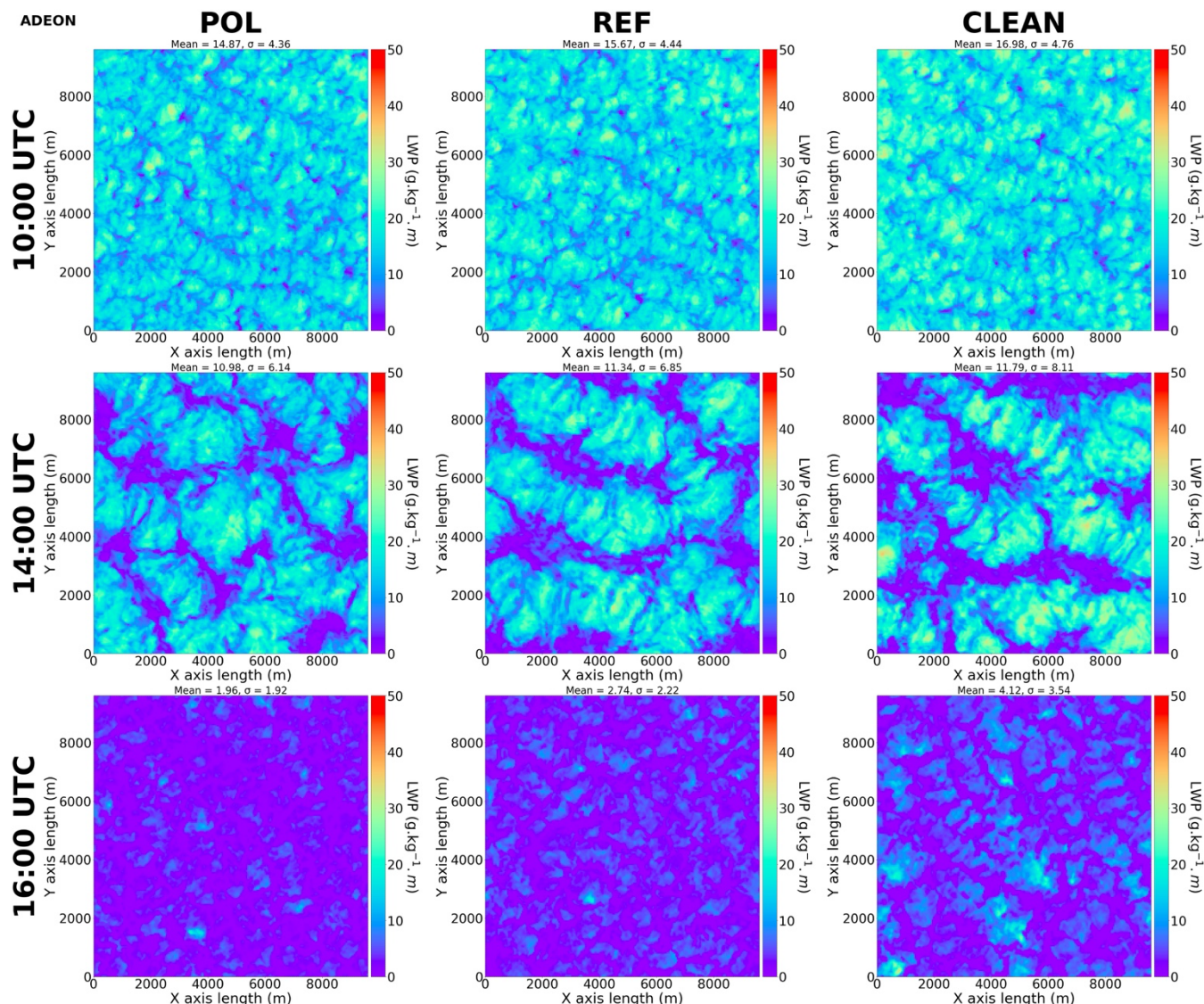


Figure 10. Evolution of cloud droplets concentration N_c (top) and cloud droplets radius r_c (middle) with the scenarios given and designated by letter a (REF), b (POL) and c (CLEAN). Bottom panel gives the evolution of mean domain SWRADSURF differences between POL or CLEAN and REF.

|730



735 **Figure 11.** Liquid water path (LWP, $g\ kg^{-1}\ m$) in POL (left column), REF (mid-column), and CLEAN (right column) runs at 10:00 UTC (top row), 14:00 UTC (middle row), and 16:00 UTC (bottom row).

740 Figure 11 shows that the major reason behind the above-described trend of SWRADSURF is the difference in cloud fraction in competing with the effect brought by different cloud reflectivity of in various runs, especially before noon when zenith angle is still high. After sunrise, the cloud top starts to rise and cloud layer becomes thicker. In the meantime, this upward development brings a downward entrainment of dry air from the temperature inversion zone above the cloud top and causes evaporation in the cloud. For a cloud with a large quantity of very small droplets as in POL and REF, the evaporation rate of droplets would exceed that in CLEAN case, thus more cloud-void spaces or a thinner cloud layer would form much easier than in the latter case. Note that a similar macrophysical response to aerosol

745 concentration variation (in a simple high versus low setting) was also suggested in a marine cloud case though with a coarse vertical resolution of 50 m (Wang *et al.*, 2003). As shown in Fig. 11 and Table 3, cloud layer in CLEAN is slightly denser than those in POL and REF while cloud-void or thin cloud pixels account for a substantially lower ratio within the domain. Thus, before noontime, cloud reflectivity seems to become the secondary factor comparing to cloud fraction in determining the value of SWRADSURF. 750 As a result, SWRADSURF in CLEAN is significantly lower than REF ~~then and~~ POL until zenith angle becomes lower closer to noontime. The lower SWRADSURF in CLEAN would also have reduced the turbulent mixing as well as delayed the convection that would cause extensive cloud break-up. At 14:00 UTC, differences in cloud thickness and cloud-void space still exists but becomes relatively smaller among the three different runs (Fig. 11 and Table 3), cloud reflectivity now becomes the primary reason 755 to cause a different SWRADSURF as shown in Fig. 10 (bottom panel). Interestingly, modeled clouds in POL and REF appear to dissipate earlier and much faster than in CLEAN in the break-up stage (Fig. 11, bottom panel).

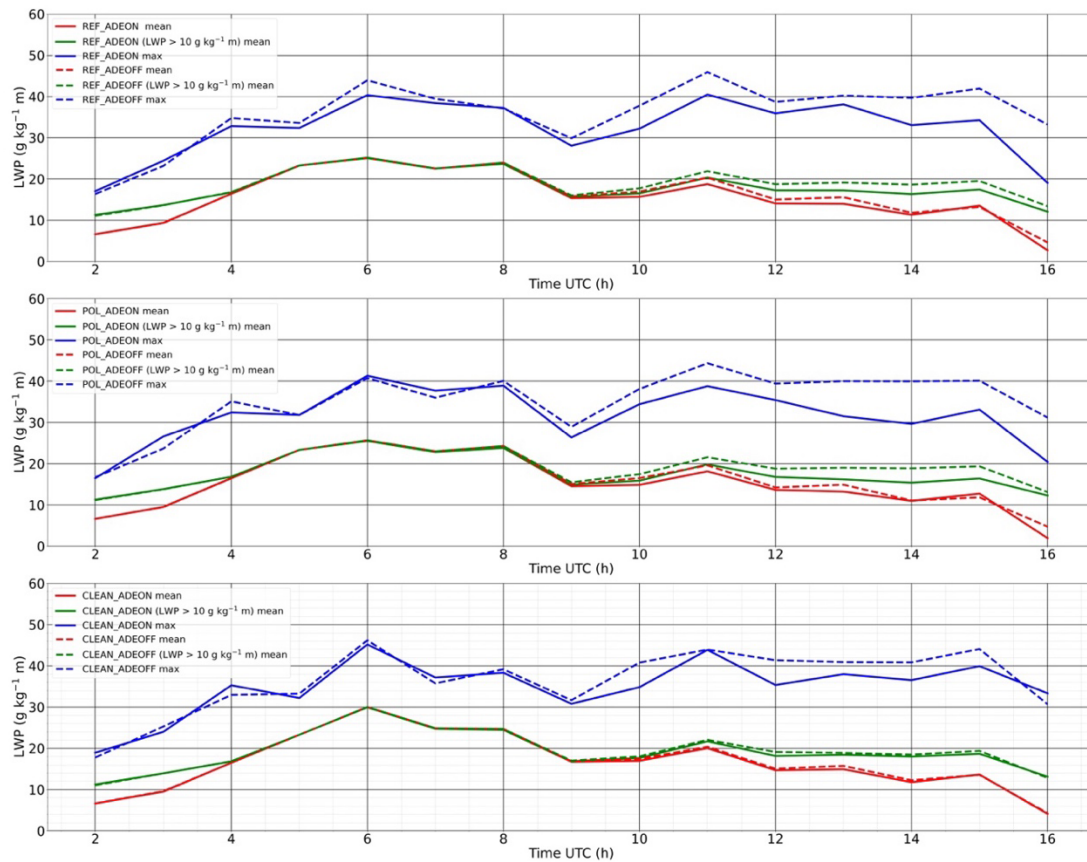
| | LWP 10 UTC | PCP 10 UTC | LWP 14 UTC | PCP 14 UTC | LWP 16 UTC | PCP 16 UTC |
|-------|------------|------------|------------|------------|------------|------------|
| POL | 14.87 | 12.79 | 10.98 | 42.17 | 1.96 | 99.66 |
| REF | 15.67 | 10.11 | 11.34 | 42.69 | 2.74 | 99.67 |
| CLEAN | 16.98 | 6.95 | 11.79 | 44.93 | 4.12 | 94.47 |

760 **Table 3.** Domain averaged liquid water path (LWP; $g\ kg^{-1}\ m$) and poor-cloud pixel percentage (PCP, defined by the percentage of pixels where LWP < 10 $g\ kg^{-1}\ m$; percentage) in three different runs.

Looking into various ~~timely-temporally~~ varying metrics of LWP in different model runs, we find that in general, LWP is inversely ~~promotional-proportional~~ to CDNC, as LWP in POL < LWP in REF < LWP in CLEAN, and this is applied to different metrics of LWP (Fig. 12, ~~ref. ADEON curves~~; Table 3) ~~as well~~. 765 However, in comparison, the peak LWP varies less significantly in CLEAN case, while peak LWPs in two other runs decrease with domain averaged quantities in convection stage. There were different opinions regarding the mechanisms behind such an inverse relation between LWP and CDNC (*e.g.*, Ackerman *et al.*, 2004; Bretherton *et al.*, 2007), not to mention that most such hypotheses were proposed based on the cases of marine low clouds that might not be directly applied to the cases over land. In our 770 analysis, the difference in turbulent mixing driven by the surface radiative heating, as influenced by different microphysical features in various cases, seems having played a critical role. The situation of cloud fraction (CF) is somewhat more complicated. As shown in Table 3 and Fig. A3, CF relation with CDNC varies in different stages. An inverse relation between CF and CDNC generally stands in the earlier and later period of the convection stage. This is primarily due to the faster evaporation of clouds with higher CDNC driven by entrainment in the former period (note the controlling role of CF in determining the surface incoming solar radiation and thus turbulence in this stage), or by strong convection in the latter. In the middle of the convection stage (13:00-15:00 UTC), the above relation, however, would reverse or become insignificant, owing to a weaker turbulent mixing in polluted cases since the cloud reflectivity becomes the dominant factor in controlling the surface incoming solar 775

780 ~~radiation as discussed previously. Therefore, an analysis throughout the entire LLSC life cycle is very~~
~~important to understand the response of CF alongside LWP to aerosol variation. Note that the atmospheric~~
~~heating caused by absorbing black carbon aerosol is already included in this series of sensitivity~~
~~simulations, though its impacts on the above result will be discussed later based on another set of~~
785 ~~sensitivity runs. The situation of cloud fraction (CF) is somewhat more complicated. As shown in Table~~
~~3 and Fig. A4, CF relation with CDNC varies in different stages. An inverse relation between CF and~~
~~CDNC generally stands in the earlier and later period of the convection stage, in the middle of the~~
~~convection stage (13:00–15:00 UTC), the above relation, however, would reverse, alongside the vertical~~
~~cloud extent as discussed previously.~~

To summarize, as expected, aerosol concentration is a major factor in controlling the cloud
790 microphysical features by determining the simulated droplet number concentration and radius ~~of clouds~~
with similar liquid water content. However, our results suggest that cloud reflectivity as a function of
CDNC is not necessarily a dominant factor to solely determine the surface incoming solar radiation
~~particularly when dynamical situation is more complicated to maintain a constant LWC.~~ Instead, the
response of cloud macrophysical features such as ~~cloud void space (or inversely, cloud fraction)~~ as well
795 as LWP to the variation caused by dry entrainment from inversion layer above the cloud is also a
competing the dominant factor in determining the incoming solar radiation at ground. Our sensitivity
simulations utilize different aerosol profiles that reflect the variations in both aerosol concentration and
chemical composition based on observations~~study weights in both size distribution and chemical~~
~~composition in aerosol variation for modeling such situations~~, the results indicate a critical role of cloud
800 microphysical response to aerosol in deciding the LWP and CF response. The overall negative response
of LWP to aerosol concentration derived here agrees with several previous studies (*e.g.*, Ackerman *et al.*,
2004; Jiang and Feingold, 2006). While the case for CF response is more complicated, varying in different
stages in cloud life cycle. It is worth indicating though, another factor that might contribute to the cloud
life cycle, *i.e.*, the atmospheric heating caused by the semi-direct effect of absorbing aerosol component
805 such as black carbon has not been analyzed up to this moment and will be discussed in the following
section.



810 **Figure 12.** Domain averaged LWP (LWP mean), maximum LWP (LWP max), and domain averaged LWP over pixels where LWP > $10 \text{ g kg}^{-1} \text{ m}$ in AODON-ADEON and AODEFF-ADEOFF runs in REF (upper panel), POL (middle panel), and CLEAN (lower panel) cases, derived using hourly model outputs.

4.32 Impact of aerosol semi-direct effect on LLSCs

815 The semi-direct effect of aerosols, resulted from SW radiation absorption by absorbing aerosol, could affect atmospheric dynamics surrounding LLSCs and thus their life cycle. ~~This To examine this effect, we have designed has been examined in our study by comparing the results of three additional experimentssensitivity simulations, constructed-configured~~ accordingly in the same way as their original experiments POL, REF, and CLEAN (hereafter ADEON of REF, POL, and CLEAN, respectively) but excluding aerosol direct effects (named ADEOFF); ~~Therefore, comparison between the ADEOFF runs with and those of the three their~~ paired original ADEON runs ~~provides information regarding the isolated impacts of the semi-direct effect on the LLSC life cycle for cases with different aerosol profiles.~~ Apparently, BC is the major species behind the semi-direct effect in our case. ~~The last one contains three experiments without aerosol semi direct effect for CLEAN, POL, and REF aerosol profiles, respectively,~~

820

825 called ADEOFF runs, which form paired simulations correspondingly with original CLEAN, POL, and REF runs, i.e., the ADEON runs of these scenarios.

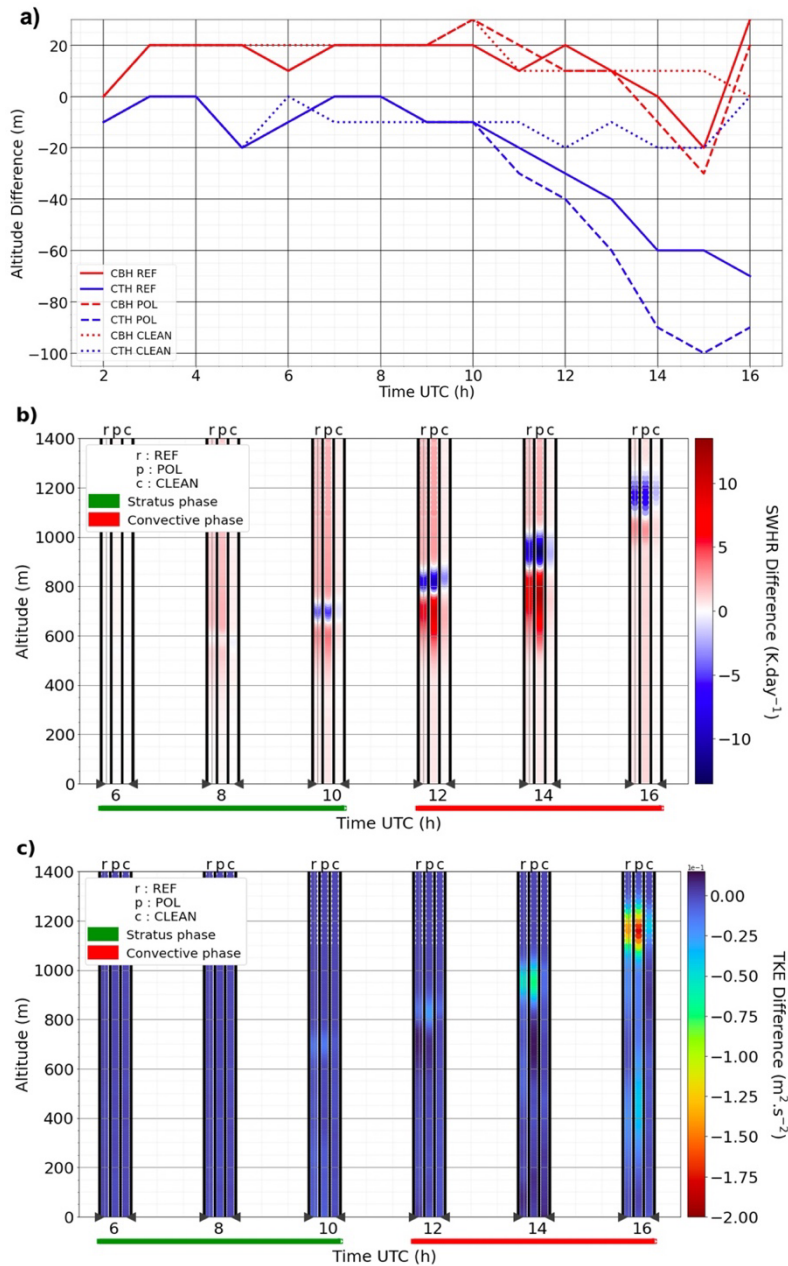
The changes in cloud top and base, SWHR, and TKE due to aerosol absorption and associated feedbacks are shown in Figure 13. The results demonstrate that light-absorbing BC aerosols can cause a substantial atmospheric heating accompanied by a warming tendency near the top of LLSCs (Fig. 830 13b). At 14:00 UTC, the domain averaged heating due to BC aerosols (difference in SWHR between ~~AODON_ADEON~~ and ~~AODOFF_ADEOFF~~) and a consequent cooling just above the cloud due mostly to the cloud top change are 12.16 K day^{-1} and $-13.14 \text{ K day}^{-1}$ in POL, and 7.71 K day^{-1} and -9.24 K day^{-1} in REF, respectively. In comparison, the atmospheric heating and associated cooling of 1.30 K day^{-1} and -2.25 K day^{-1} in CLEAN case are clearly insignificant. Accordingly, in ADEON runs, more water vapor 835 tends to condense onto cloud droplets under the higher relative humidity in the lower PBL and decreasing turbulent mixing (Fig. 13c, with a maximum decreasing of $-0.18 \text{ m}^2 \text{ s}^{-2}$ for POL), leading to a decrease of the cloud top height, limiting entrainment, and ~~also~~ reducing incoming solar radiation at surface due to BC in-cloud absorption. The cloud top height reduction due to the semi-direct effect in two polluted cases POL and REF is quite substantial as shown in Figure 13a, where CTH in POL and 840 REF has decreased by up to 100 and 70 meters due to the presence of BC, respectively. On the other hand, CBH ~~has~~ also increased about 20 meters in both cases before break-up, suggesting a thinner cloud layer owing to the semi-direct effect. In comparison, CTH, CBH, and thus cloud vertical extent appears to be less affected in CLEAN run due to its low BC content. Before break-up, in-cloud TKE below the heating layer has been reduced in some extent (Fig. 13c). On the other hand, due to a lower cloud top in 845 the polluted cases, planetary boundary layer height would also be lowered. The effect of BC absorption in lowering modeled cloud top and thinning cloud layer in POL and REF (implying a reduced upward development) is likely another factor to slow down their break-up as discussed before.

The impact of the semi-direct effect on other critical macrophysical features such as cloud fraction and LWP can be also seen from the model results. For instance, LWP particularly the maximum LWP is 850 clearly lower in the ~~AODON_ADEON~~ runs of the two polluted cases (REF and POL) (Fig. 12). In addition, an increase of cloud fraction due to the semi-direct effect can be seen throughout the convection stage until 15:00 UTC when massive cloud break-up occurs (Fig. ~~A4A3~~). All these imply a critical role of the semi-direct effect on cloud radiation.

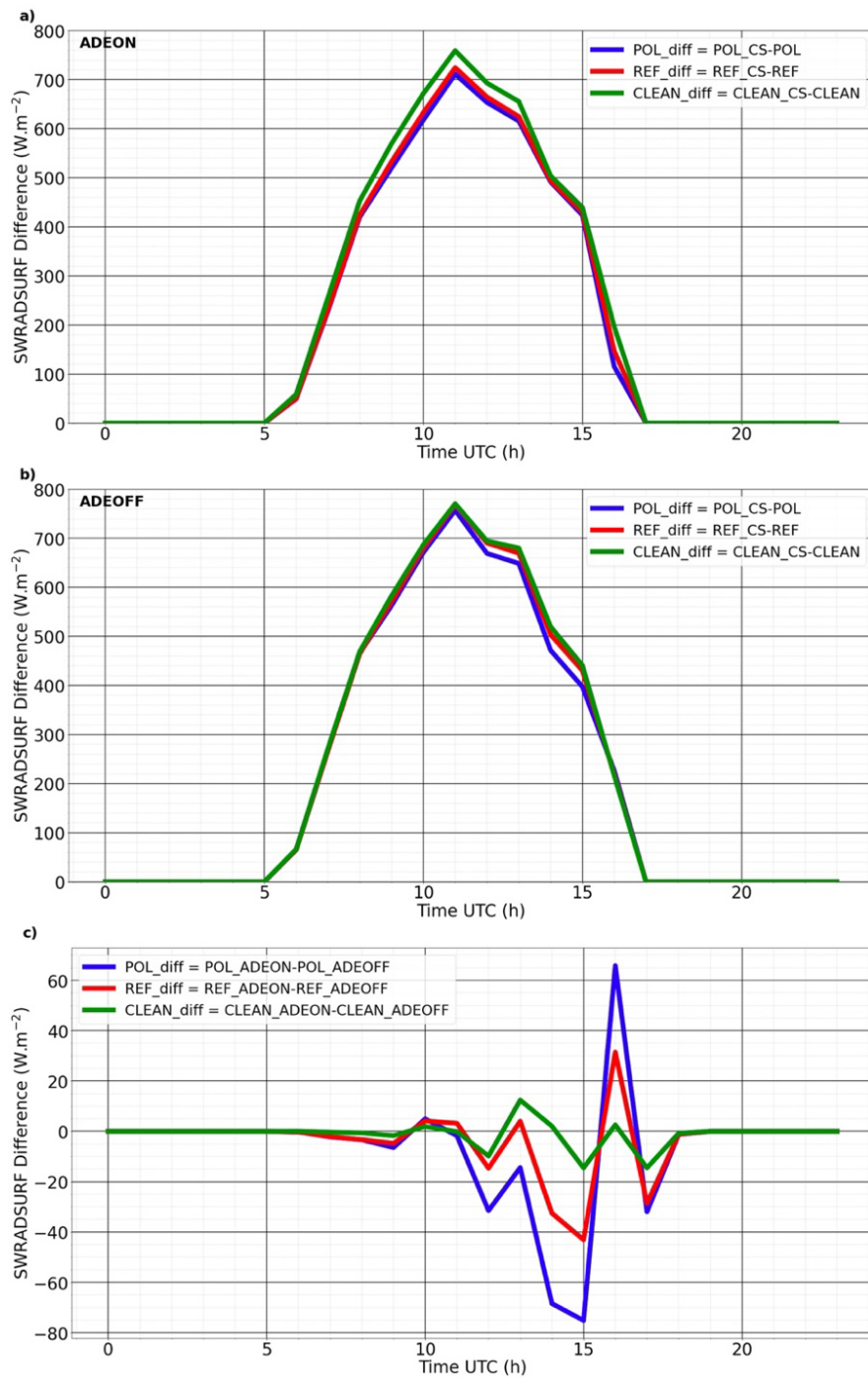
We find that the semi-direct effect can both enhance and weaken the (negative) indirect radiative 855 forcing as also indicated by some previous works (Lohmann and Feichter, 2001; Koch and Del Genio, 2010a; Huang *et al.*, 2014; Yamaguchi *et al.*, 2015; Stjern *et al.*, 2017; Kreidenweis *et al.*, 2019; ~~Zhang and Zuidema, 2019~~). In the convection stage before 15:00 UTC, the difference in SWRADSURF between ADEON and ADEOFF is negative, reaching -33 W m^{-2} and -75 W m^{-2} for REF and POL at 14:00 UTC, respectively (Fig. 14c). This can be explained by an increase in cloud fraction in ADEON runs (Fig. 860 ~~A4A3~~, Table 3) that allows less solar irradiance to attain the surface despite the cloud layer being thinner, not to mention that solar irradiance itself has already been reduced due to BC absorption (Fig. 12, 14c and ~~A23~~). Note that the different chemical compositions between POL and REF also lead to a quantitatively different effect. Hence, the semi-direct effect contributes positively to the enhancement of (negative) indirect radiative forcing in this case. On the other hand, at 16:00 UTC, the flux difference

865 between ADEON and ADEOFF becomes positive with values for REF and POL as 32 W m^{-2} and 66 W m^{-2} , respectively. As the clouds break up more slowly in ADEOFF during this stage due to thicker cloud layers (Fig. A23 and A34), more clouds inside the domain with increased thickness causes weaker SW irradiance reaching the ground. In other words, the semi-direct effect makes the cloud dissipate faster in the later convective stage. In this case, the semi-direct effect weakens the ~~semidirect~~indirect radiative
870 forcing.

The above results have demonstrated the important role of solar absorption by aerosols in determining the life cycle of LLSCs. ~~The atmospheric heating by light absorbing BC would limit the elevation of cloud top, especially during the break-up stage (Koeh and Del Genio, 2010b; Zhang and Zuidema, 2019). Such a heating can also increase cloud fraction then delay break-up until late afternoon, especially for clouds with higher cloud droplet number concentration in polluted environment such as in POL and REF runs (opposite to the outcome by considering aerosol number concentration only), and thus affect the indirect effect of aerosols.~~ Note that our modeling configurations are based on the aerosol profiles that are relatively well-mixed throughout the PBL then with concentration gradually decreasing along altitude above PBL. Certain previous sensitivity experiments suggested that the location of BC
880 layer within or above PBL could have different impacts on the development of convection, entrainment, and thus life cycle of the low clouds within PBL. For instance, Johnson *et al.* (2004) suggested that without considering the indirect effect of aerosols, BC existing within boundary layer would lower LWP by nearly 20% in a marine low stratocumulus case, where the cloud response is less sensitive to the change in surface shortwave heating ~~ehange~~ comparing to the situation in our case. Feingold *et al.* (2005)
885 found that smoke plumes containing BC near the surface would reduce the cloudiness through both the atmospheric heating and the weakening effect on surface heat fluxes by BC. These results though obtained with somewhat different model configurations than ours (e.g., coarser vertical resolution, different surface, etc.) are in a qualitative agreement with our findings. Nevertheless, the unique configuration of our model allows us to quantitatively examine the semi-direct effect with varying aerosol
890 chemical compositions and thus extent of aerosol absorption. This has led us to reveal further insights of the complicated interplays among various aerosol effects besides their individual impacts on the life cycle of LLSCs.



895 **Figure 13.** Evolution of the difference of the mean CBH and CTH (a), SWHR (b) and TKE (c) between the simulation runs with and without aerosol direct effect (ADEON-ADEOFF) for REF, POL and CLEAN.



900

Figure 14. Mean difference surface SW radiative flux (SWRADSURF) between Clear-Sky (CS) and cloudy scenarios giving the flux dissipated by clouds in ADEON (a) and ADEOFF (b) configurations. SWRADSURF difference between ADEON and ADEOFF configuration for the three scenarios (c).

905 5. Conclusions

An ~~characteristic-observed LLSC~~ case ~~of the LLSCs~~ over southern West Africa has been simulated with Meso-NH model in a Large-Eddy Simulation configuration constrained by the measurements from ~~the~~-DACCIWA field campaign. The model has successfully reproduced the observed nocturnal-to-diurnal life cycle alongside key macro- and microphysical features as well as surface radiative and heat fluxes. To determine the impact of aerosols on the modeled life cycle of LLSCs, sensitivity simulations using several different aerosol profiles as well as the ones adopting these profiles but excluding the aerosol direct radiation effect have also been conducted. These aerosol profiles contain different size distributions and chemical compositions, reflecting the situations associated with various aerosol populations encountered during the field campaign.

915 The results from ~~various~~-sensitivity simulations suggest that both aerosol size distribution and chemical composition can effectively influence the LLSCs life cycle. The impact of the aerosol size distribution, as reflected from a comparison among simulations using aerosol profiles with different number concentrations and modal distributions, is initiated from resultant cloud microphysical features in particular the cloud droplet number concentration and mean droplet size. Such a difference created by different aerosol size distributions also affect cloud reflectivity as expected. Interestingly, we have found that the difference in cloud reflectivity caused by different aerosol concentration does not always dominate the surface incoming solar radiation and thus cloud development after sunrise. This is due to a competing factor: the difference in cloud fraction caused by the resulted from different evaporation speed of cloud droplets (a function of CDNC) due to the dry air entrained from the inversion layer above cloud top ~~and associated evaporation of cloud droplets as a function of CDNC~~, which specifically dominates the variation of surface incoming solar radiation before noontime. Clouds influenced by higher aerosol concentrations and thus having higher number concentration and smaller sizes of cloud droplets are found to evaporate more easily and thus impose a lower cloud fraction. For the same reason, clouds with higher droplet concentration are likely to break up earlier.

930 In addition, our sensitivity runs including versus excluding aerosol direct radiative effects have also demonstrated the impact specifically of solar absorption by black carbon on the cloud life cycle. The excessive atmospheric heating reaching $12 K day^{-1}$ introduced by black carbon in our modeled cases is found to be able to lower the cloud top height as well as liquid water path, reduce dry entrainment, and increase cloud fraction. Working with the cloud fraction response to aerosol size distribution, this heating and its consequences might delay break-up of the LLSCs until late afternoon. All these would enhance the aerosol indirect effect. While-On the other hand, beyond that point, the modeled clouds in polluted cases with higher aerosol concentrations and BC ~~included-content~~ would break up faster in late afternoon due to their thinner cloud layers. ~~Therefore, the semi-direct effect can contribute positively to the indirect radiative forcing (negative in quantity) by increasing cloud fraction, or negatively by causing thinner cloud layer and thus a faster cloud break-up in late afternoon, all depending on the phase in stratiform cloud life cycle as demonstrated in this study and several previous ones~~In this case the semi-direct effect would weaken the indirect effect.

940 Our study has demonstrated that the life cycle and thus the radiative forcing of LLSCs over land area of SWA can be substantially influenced by aerosols from both long-range transported biomass

945 burning plumes and from local anthropogenic emissions. In fact, more aerosol profiles had been
collected during ~~the~~ DACCIWA campaign besides the ones used in this study. Future research works
could reveal the aerosol impact under an even broader range of aerosol properties and to examine the
temporal variations of LLSCs radiative effects evolving with different large-scale meteorological
conditions with different associated air mass. More analysis on different cloud cases in SWA would also
950 be able to assess or refute current results on semi-direct effect.

Code and data availability. The data obtained during ~~the~~ DACCIWA campaign at the Savè supersite
955 alongside all other data used in this study are publicly available on the SEDOO database
(<http://baobab.sedoo.fr/DACCIWA/>). The Meso-NH code is maintained and updated by LAERO and
CNRM, it is freely available for download at <http://mesonh.aero.obs-mip.fr/mesonh52/>.

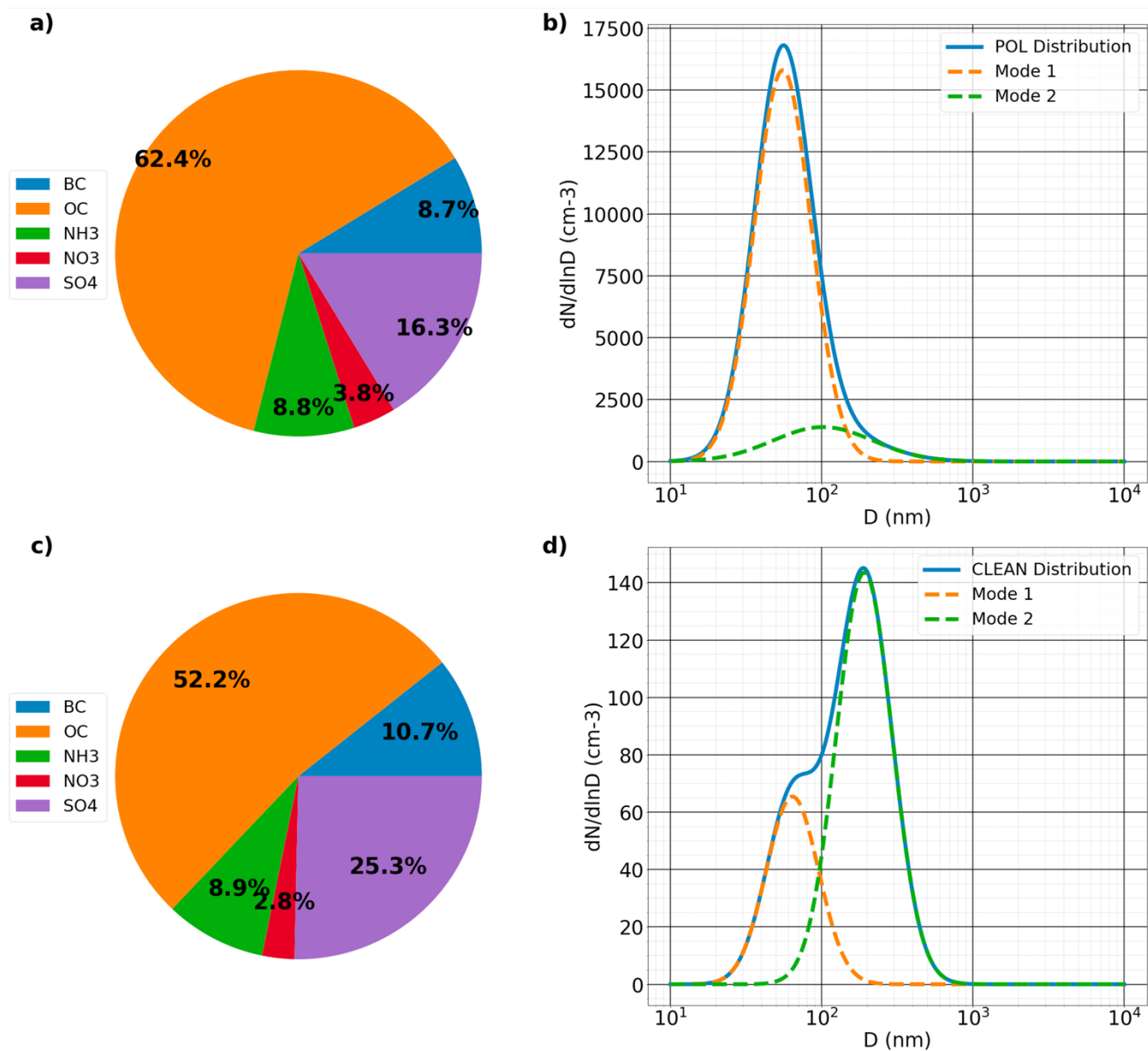
Author contributions. LD and CW designed the simulations and LD conducted model simulations and
960 data analyses. LD and CW wrote this paper with contribution from all other co-authors. CW advised and
helped LD to better understand the different aspects of this research work. PT advised and trained LD ~~for~~
to use Meso-NH and ORILAM module ~~use~~. CD processed and provided the aerosol profiles used in
previous simulations and NM was part of this work. MZ helped to select the study case and advised
during the study case construction and analysis. AD brought a critical eye to this work.

965 **Competing interests.** The authors declare that they have no conflict of interest.

Acknowledgements. This study is supported by L'Agence National de la Recherche (ANR) of France
under "Programme d'Investissements d'Avenir" (ANR-18-MPGA-003 EUROACE) and co-funded by
970 the University of Toulouse III Paul Sabatier. The computation of this work was performed using HPC
resources of French GENCI-IDRIS (Grant A0110110967 and A0090110967) and French Regional
Computations center CALMIP. LD thanks the Laboratoire d'Aérodynamique, Université de Toulouse, France,
for funding and hosting his Ph.D. research activities. LD also thanks the Meso-NH team, especially
975 Quentin Rodier, Juan Escobar, and Philippe Wautelet, for their advises on using Meso-NH, Benoit Vié
and Marie Mazoyer for their help to handle and modify microphysical scheme LIMA, Quentin Libois for
explaining the details of Meso-NH's radiative schemes, and specifically Fabienne Lohou (LAERO) for
her introduction of DACCIWA campaign alongside her guidance in using relevant data products. A
special thanks the authors to all people whose work was involved in the measurement and processing of
980 DACCIWA campaign data especially over the Savè supersite. Many constructive comments and
suggestions from Dr. Mónica Zamora Zapata and an anonymous reviewer as well as the handling editor,
Dr. Graham Feingold have made a substantial impact on our effort to improve the quality of the
manuscript.

985

Appendix A



990 **Figure A1.** Mass composition (a,c) and size distribution provided by (Denjean et al., 2020a) and fitted into 2 modes described in Table 2 (b,d) for scenarios POL (top), CLEAN (bottom).

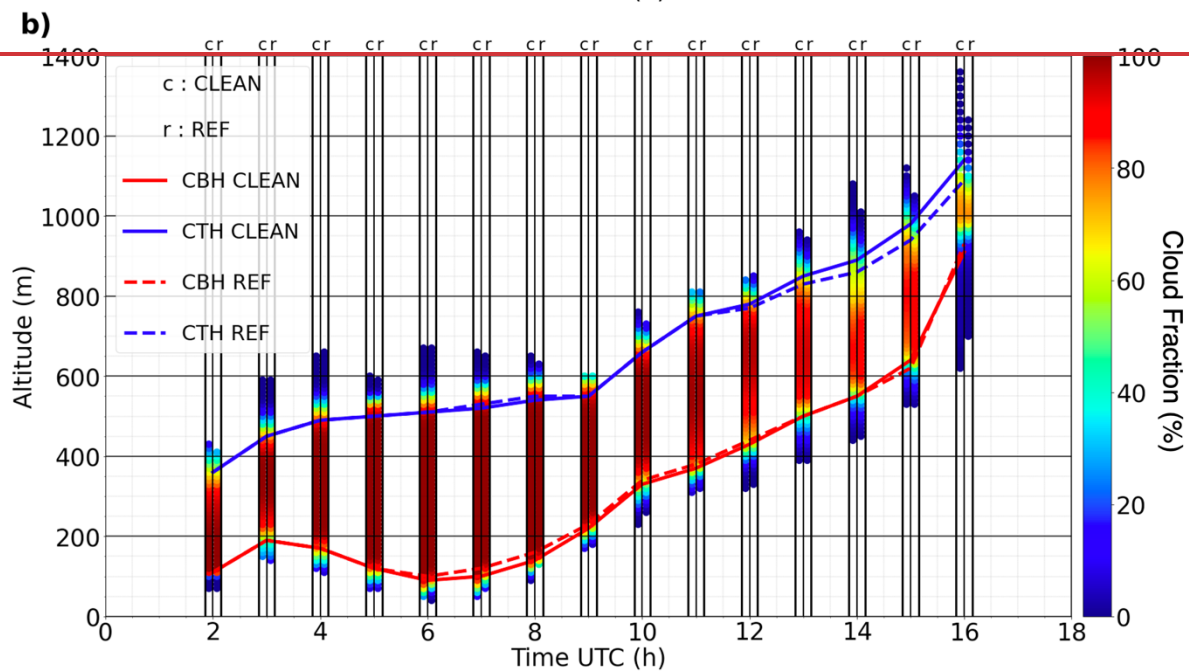
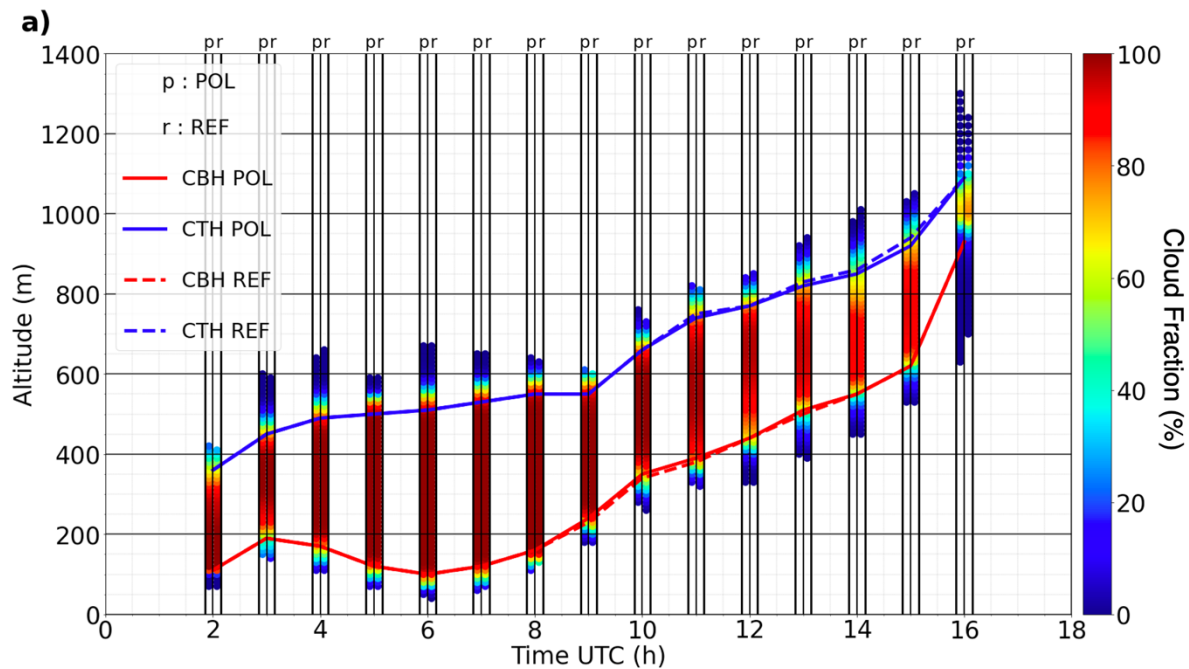


Figure A2. Mean LLSCs deck evolution of POL (a) and CLEAN (b) cases with the representation of REF's one to make comparison and REF_NOBC ADEON and ADEOFF runs (c), vertical color bars for POL/CLEAN (left) and REF (right) attribute at each altitude level a cloud presence density for both cases at each hour.

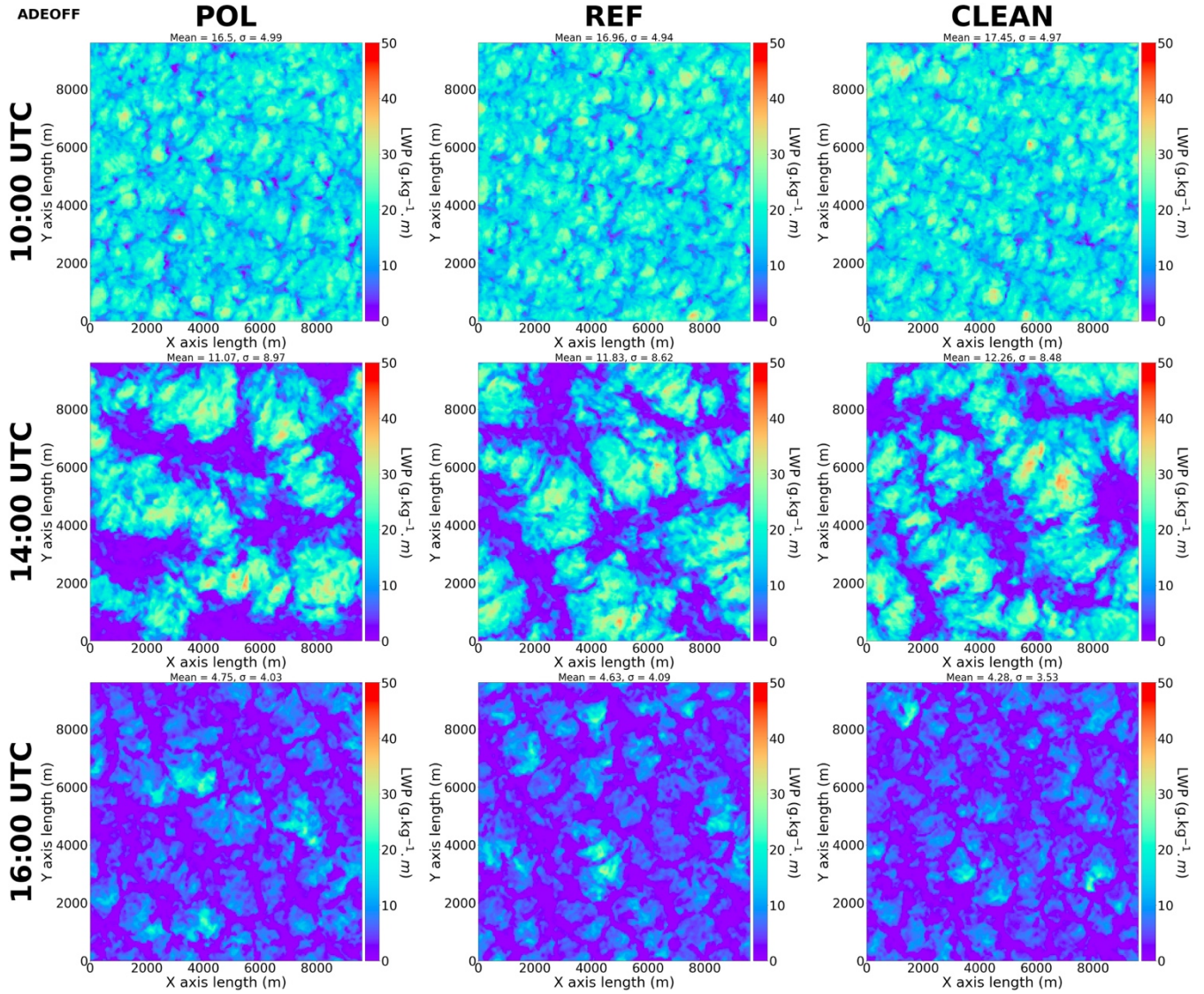


Figure A3A2. Liquid water path (LWP, $g\ kg^{-1}\ m$) in POL (left column), REF (mid-column), and CLEAN (right column) ADEOFF runs at 10:00 UTC (top row), 14:00 UTC (middle row), and 16:00 UTC (bottom row).

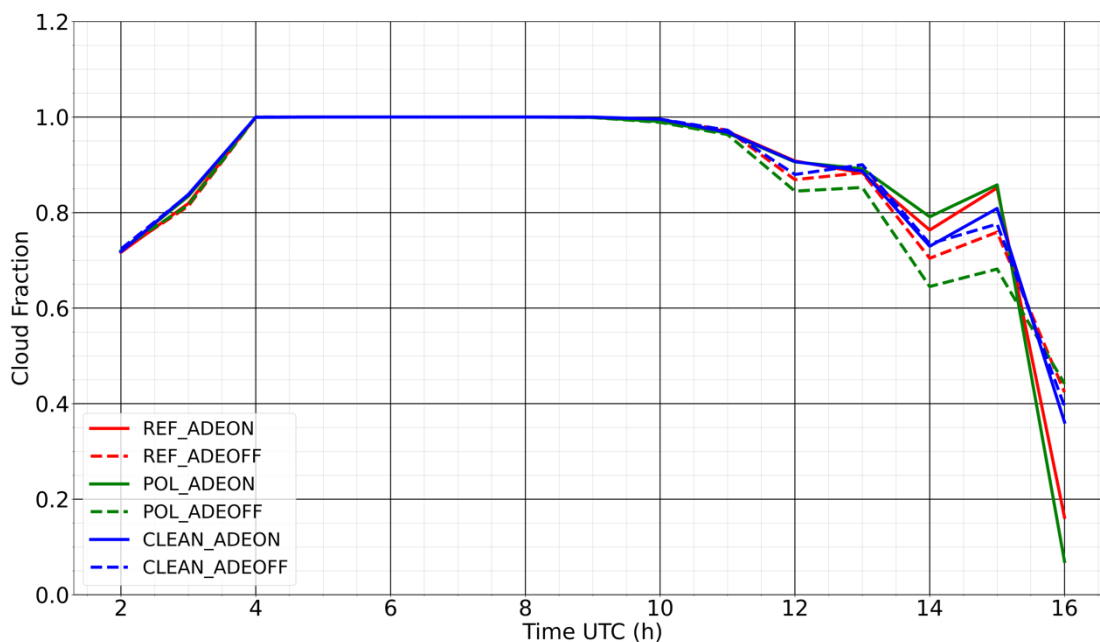


Figure A4A3. Domain averaged cloud fraction for AODON (solid lines) and AODOFF (dotted lines) of REF (red), POL (green), and CLEAN (blue) cases, derived using hourly model outputs. The cloud fraction here is a column quantity, defined as pixels where $LWP > 5 \text{ g kg}^{-1} \text{ m}$.

1010

References

- Abdul-Razzak, H. and Ghan, S. J.: A parameterization of aerosol activation: 2. Multiple aerosol types, *J. Geophys. Res.-Atmos.*, 105, 6837–6844, <https://doi.org/10.1029/1999JD901161>, 2000.
- 1015 Abdul-Razzak, H. and Ghan, S. J.: Parameterization of the influence of organic surfactants on aerosol activation, *J. Geophys. Res.-Atmos.*, 109, <https://doi.org/10.1029/2003JD004043>, 2004.
- Ackerman, A. S., Kirkpatrick, M. P., Stevens, D. E., and Toon, O. B.: The impact of humidity above stratiform clouds on indirect aerosol climate forcing, *Nature*, 432, 1014–1017, <https://doi.org/10.1038/nature03174>, 2004.
- 1020 Adler, B., Babic, K., Kalthoff, N., Lohou, F., Lothon, M., Dione, C., Pedruzo-Bagazgoitia, X., and Andersen, H.: Nocturnal low-level clouds in the atmospheric boundary layer over southern West Africa: an observation-based analysis of conditions and processes, *Atmos. Chem. Phys.*, 19, 663–681, <https://doi.org/10.5194/acp-19-663-2019>, 2019.
- Aouizerats, B., Thouron, O., Tulet, P., Mallet, M., Gomes, L., and Henzing, J. S.: Development of an online radiative module for the computation of aerosol optical properties in 3-D atmospheric models: validation during the EUCAARI campaign, *Geoscientific Model Development*, 3, 553–564, <https://doi.org/10.5194/gmd-3-553-2010>, 2010.
- 1025 Babic, K., Adler, B., Kalthoff, N., Andersen, H., Dione, C., Lohou, F., Lothon, M., and Pedruzo-Bagazgoitia, X.: The observed diurnal cycle of low-level stratus clouds over southern West Africa: a case study, *Atmos. Chem. Phys.*, 19, 1281–1299, <https://doi.org/10.5194/acp-19-1281-2019>, 2019.
- Bauer, S. E., Im, U., Mezuman, K., and Gao, C. Y.: Desert Dust, Industrialization, and Agricultural Fires: Health Impacts of Outdoor Air Pollution in Africa, *J. Geophys. Res.-Atmos.*, 124, 4104–4120, <https://doi.org/10.1029/2018JD029336>, 2019.
- 1030

- Bellon, G. and Stevens, B.: Time Scales of the Trade Wind Boundary Layer Adjustment, *J. Atmos. Sci.*, 70, 1071 – 1083, <https://doi.org/10.1175/JAS-D-12-0219.1>, 2013.
- 1035 Boucher, O., D. Randall, P. Artaxo, C. Bretherton, G. Feingold, P. Forster, V.-M. Kerminen, Y. Kondo, H. Liao, U. Lohmann, P. Rasch, S.K. Satheesh, S. Sherwood, B. Stevens, and X.Y. Zhang: Clouds and Aerosols. In: Climate Change 2013: The Physical Science Basis. Contribution of Working Group I to the Fifth Assessment Report of the Intergovernmental Panel on Climate Change [Stocker, T.F., D. Qin, G.-K. Plattner, M. Tignor, S.K. Allen, J. Boschung, A. Nauels, Y. Xia, V. Bex and P.M. Midgley (eds.)]. Cambridge University Press, Cambridge, United Kingdom and New York, NY, USA, 2013.
- 1040 Bretherton, C. S., Blossy, F. N., and Uchida, J. : Cloud droplet sedimentation, entrainment efficiency, and subtropical stratocumulus albedo, *Geophys. Res. Lett.*, 34, L03813, doi:10.1029/2006GL027648, 2007.
- Brito, J., Freney, E., Dominutti, P., Borbon, A., Haslett, S. L., Batenburg, A. M., Colomb, A., Dupuy, R., Denjean, C., Burnet, F., Bourriane, T., Deroubaix, A., Sellegri, K., Borrmann, S., Coe, H., Flamant, C., Knippertz, P., and Schwarzenboeck, A.: Assessing the role of anthropogenic and biogenic sources on PM₁ over southern West Africa using aircraft measurements, *Atmos. Chem. Phys.*, 18, 757–772, <https://doi.org/10.5194/acp-18-757-2018>, 2018.
- 1045 Caniaux, G., Redelsperger, J.-L., and Lafore, J.-P.: A Numerical Study of the Stratiform Region of a Fast-Moving Squall Line. Part I: General Description and Water and Heat Budgets, *J. Atmos. Sci.*, 51, 2046 – 2074, [https://doi.org/10.1175/15200469\(1994\)051<2046:ANSOTS>2.0.CO;2](https://doi.org/10.1175/15200469(1994)051<2046:ANSOTS>2.0.CO;2), 1994.
- 1050 Carslaw, K. S., Gordon, H., Hamilton, D. S., Johnson, J. S., Regayre, L. A., Yoshioka, M., and Pringle, K. J.: Aerosols in the Pre-industrial Atmosphere, *Current Climate Change Reports*, 3, 1–15, <https://doi.org/10.1007/s40641-017-0061-2>, 2017.
- Chatfield, R. B., Vastano, J. A., Li, L., Sachse, G. W., and Connors, V. S.: The Great African Plume from biomass burning: Generalizations from a three-dimensional study of TRACE A carbon monoxide, *J. Geophys. Res.-Atmos.*, 103, 28059–28077, <https://doi.org/https://doi.org/10.1029/97JD03363>, 1998.
- 1055 Chen, T., Rossow, W. B., and Zhang, Y.: Radiative Effects of Cloud-Type Variations, *J. Clim.*, 13, 264 – 286, [https://doi.org/10.1175/1520-0442\(2000\)013<0264:REOCTV>2.0.CO;2](https://doi.org/10.1175/1520-0442(2000)013<0264:REOCTV>2.0.CO;2), 2000.
- Cleveland, W. S.: Robust Locally Weighted Regression and Smoothing Scatterplots, *Journal of the American Statistical Association*, 74, 829–836, <https://doi.org/10.1080/01621459.1979.10481038>, 1979.
- Cohard, J.-M. and Pinty, J.-P.: A comprehensive two-moment warm microphysical bulk scheme. I: Description and tests, *Quar. J. Roy. Meteorol. Soc.*, 126, 1815–1842, <https://doi.org/https://doi.org/10.1002/qj.49712656613>, 2000.
- 1060 Dearden, C., Hill, A., Coe, H., and Choularton, T.: The role of droplet sedimentation in the evolution of low-level clouds over southern West Africa, *Atmos. Chem. Phys.*, 18, 14253–14269, <https://doi.org/10.5194/acp-18-14253-2018>, 2018.
- 1065 Deetz, K., Vogel, H., Knippertz, P., Adler, B., Taylor, J., Coe, H., Bower, K., Haslett, S., Flynn, M., Dorsey, J., Crawford, I., Kottmeier, C., and Vogel, B.: Numerical simulations of aerosol radiative effects and their impact on clouds and atmospheric dynamics over southern West Africa, *Atmos. Chem. Phys.*, 18, 9767–9788, <https://doi.org/10.5194/acp-18-9767-2018>, 2018.
- Denjean, C., Bourriane, T., Burnet, F., Mallet, M., Maury, N., Colomb, A., Dominutti, P., Brito, J., Dupuy, R., Sellegri, K., Schwarzenboeck, A., Flamant, C., and Knippertz, P.: Overview of aerosol optical properties over southern West Africa from DACCIIWA aircraft measurements, *Atmos. Chem. Phys.*, 20, 4735–4756, <https://doi.org/10.5194/acp-20-4735-2020>, 2020a.
- 1070 Denjean, C., Brito, J., Libois, Q., Mallet, M., Bourriane, T., Burnet, F., Dupuy, R., Flamant, C., and Knippertz, P.: Unexpected Biomass Burning Aerosol Absorption Enhancement Explained by Black Carbon Mixing State, *Geophys. Res. Lett.*, 47, e2020GL089055, <https://doi.org/https://doi.org/10.1029/2020GL089055>, e2020GL089055, 2020b.
- 1075 Deroubaix, A., Menut, L., Flamant, C., Brito, J., Denjean, C., Dreiling, V., Fink, A., Jambert, C., Kalthoff, N., Knippertz, P., Ladkin, R., Mailler, S., Maranan, M., Pacifico, F., Pigué, B., Siour, G., and Turquety, S.: Diurnal cycle of coastal anthropogenic pollutant transport over southern West Africa during the DACCIIWA campaign, *Atmos. Chem. Phys.*, 19, 473–497, <https://doi.org/10.5194/acp-19-473-2019>, 2019.
- Deroubaix, A., Menut, L., Flamant, C., Knippertz, P., Fink, A. H., Batenburg, A., Brito, J., Denjean, C., Dione, C., Dupuy, R., Hahn, V., Kalthoff, N., Lohou, F., Schwarzenboeck, A., Siour, G., Tuccella, P., and Voigt, C.: Sensitivity of low-

- 1080 level clouds and precipitation to anthropogenic aerosol emission in southern West Africa: a DACCIWA case study, *Atmos. Chem. Phys.*, 22, 3251–3273, <https://doi.org/10.5194/acp-22-3251-2022>, 2022.
- Derrien, S., Bezombes, Y., Bret, B., Gabella, O., Jarnot, C., Medina, P., Piques, E., Delon, C., Dione, C., Campistron, B., Durand, P., Jambert, C., Lohou, F., Lothon, M., Pacifico, F., and Meyerfeld, Y.: DACCIWA field campaign, Savè super-site, UPS instrumentation, 10.6096/DACCIWA.1618, 2016.
- 1085 Dione, C., Lohou, F., Lothon, M., Adler, B., Babic, K., Kalthoff, N., Pedruzo-Bagazgoitia, X., Bezombes, Y., and Gabella, O.: Low-level stratiform clouds and dynamical features observed within the southern West African monsoon, *Atmos. Chem. Phys.*, 19, 8979–8997, <https://doi.org/10.5194/acp-19-8979-2019>, 2019.
- Eastman, R. and Warren, S. G.: Diurnal Cycles of Cumulus, Cumulonimbus, Stratus, Stratocumulus, and Fog from Surface Observations over Land and Ocean, *J. Clim.*, 27, 2386 – 2404, <https://doi.org/10.1175/JCLI-D-13-00352.1>, 2014.
- 1090 Feingold, G., Jiang, H. L., and Harrington, J. Y.: On smoke suppression of clouds in Amazonia, *Geophys. Res. Lett.*, 32, 804, doi: 10.1029/2004GL021369, 2005.
- Flamant, C., Deroubaix, A., Chazette, P., Brito, J., Gaetani, M., Knippertz, P., Fink, A. H., de Coetlogon, G., Menut, L., Colomb, A., Denjean, C., Meynadier, R., Rosenberg, P., Dupuy, R., Dominutti, P., Duplissy, J., Bourriane, T., Schwarzenboeck, A., Ramonet, M., and Totems, J.: Aerosol distribution in the northern Gulf of Guinea: local
- 1095 anthropogenic sources, long-range transport, and the role of coastal shallow circulations, *Atmos. Chem. Phys.*, 18, 12363–12389, <https://doi.org/10.5194/acp-18-12363-2018>, 2018.
- Flossmann, A. I. and Wobrock, W.: Cloud Processing of Aerosol Particles in Marine Stratocumulus Clouds, *Atmosphere*, 10, <https://doi.org/10.3390/atmos10090520>, 2019.
- Fouquart, Y. and Bonnel, B.: Computations of solar heating of the earth’s atmosphere – A new parameterization, *Beitrag zur Physik der Atmosphäre*, 53, 35-62, 1980.
- 1100 Geoffroy, O., Brenguier, J.-L., and Sandu, I.: Relationship between drizzle rate, liquid water path and droplet concentration at the scale of a stratocumulus cloud system, *Atmos. Chem. Phys.*, 8, 4641–4654, <https://doi.org/10.5194/acp-8-4641-2008>, 2008.
- Ghonima, M., Heus, T., Norris, J. R., and J. Kleissl, J.: Factors controlling stratocumulus cloud lifetime over coastal land, *J. Atmos. Sci.*, 73, 2961-2983, 2016.
- 1105 Griffin, R. J., Nguyen, K., Dabdub, D., and Seinfeld, J. H.: A Coupled Hydrophobic-Hydrophilic Model for Predicting Secondary Organic Aerosol Formation, *J. Atmos. Chem.*, 44, 171–190, <https://doi.org/10.1023/A:1022436813699>, 2003.
- Hagan, H. D., Thompson, B., Palmo, J., and Ruskowski, A.: py-smps, <https://github.com/quant-aa/py-smps>, 2022.
- 1110 Handwerker, J., Scheer, S., and Gamer, T.: DACCIWA field campaign, Savè super-site, Cloud and precipitation, <https://doi.org/10.6096/daccciwa.1686>, 2016.
- Hannak, L., Knippertz, P., Fink, A. H., Kniffka, A., and Pante, G.: Why Do Global Climate Models Struggle to Represent Low-Level Clouds in the West African Summer Monsoon?, *J. Clim.*, 30, 1665 – 1687, <https://doi.org/10.1175/JCLI-D-16-0451.1>, 2017.
- 1115 Hansen, J., M. Sato, R. Ruedy, A. Lacis, and V. Oinas, Global warming in the twenty-first century: An alternative scenario. *PNAS*, 97, 9875-9880, 1998.
- Hartmann, D. L., Ockert-Bell, M. E., and Michelsen, M. L.: The Effect of Cloud Type on Earth’s Energy Balance: Global Analysis, *J. Clim.*, 5, 1281 – 1304, [https://doi.org/10.1175/1520-0442\(1992\)005<1281:TEOCTO>2.0.CO;2](https://doi.org/10.1175/1520-0442(1992)005<1281:TEOCTO>2.0.CO;2), 1992.
- 1120 Haslett, S. L., Taylor, J. W., Evans, M., Morris, E., Vogel, B., Dajuma, A., Brito, J., Batenburg, A. M., Borrmann, S., Schneider, J., Schulz, C., Denjean, C., Bourriane, T., Knippertz, P., Dupuy, R., Schwarzenböck, A., Sauer, D., Flamant, C., Dorsey, J., Crawford, I., and Coe, H.: Remote biomass burning dominates southern West African air pollution during the monsoon, *Atmos. Chem. Phys.*, 19, 15217–15234, <https://doi.org/10.5194/acp-19-15217-2019>, 2019.
- Haywood, J. and Boucher, O.: Estimates of the direct and indirect radiative forcing due to tropospheric aerosols: A review, *Rev. Geophys.*, 38, 513–543, <https://doi.org/https://doi.org/10.1029/1999RG000078>, 2000.
- 1125 Hill, P. G., Allan, R. P., Chiu, J. C., Bodas-Salcedo, A., and Knippertz, P.: Quantifying the Contribution of Different Cloud Types to the Radiation Budget in Southern West Africa, *J. Clim.*, 31, 5273 – 5291, <https://doi.org/10.1175/JCLI-D-17-0586.1>, 2018.

- 1130 Huang, J., Wang, T., Wang, W., Li, Z., and Yan, H.: Climate effects of dust aerosols over East Asian arid and semiarid regions, *J. Geophys. Res.-Atmos.*, 119, 11,398–11,416, <https://doi.org/https://doi.org/10.1002/2014JD021796>, 2014.
- Jiang, G.-S. and Shu, C.-W.: Efficient Implementation of Weighted ENO Schemes, *J. Comp. Phys.*, 126, 202–228, <https://doi.org/https://doi.org/10.1006/jcph.1996.0130>, 1996.
- 1135 Jiang, H., Cotton, W. R., and Feingold, G.: Simulations of aerosol-cloud-dynamical feedbacks resulting from entrainment of aerosol into the marine boundary layer during the Atlantic Stratocumulus Transition Experiment, *J. Geophys. Res.*, 107, 4813, doi:10.1029/2001JD001502, 2002.
- Jiang, H., and Feingold, G.: Effect of aerosol on warm convective clouds: Aerosol-cloud-surface flux feedbacks in a new coupled large eddy model, *J. Geophys. Res.*, 111, doi:10.1029/2005JD006138, 2006.
- Johnson, B. T., Shine, K. P., and Forster, P. M.: The semi-direct aerosol effect: Impact of absorbing aerosols on marine stratocumulus, *Q. J. R. Meteorol. Soc.*, 130, 1407-1422, 2004.
- 1140 Kalthoff, N., Lohou, F., Brooks, B., Jegede, G., Adler, B., Babic, K., Dione, C., Ajao, A., Amekudzi, L. K., Aryee, J. N. A., Ay'oola, M., Bessardon, G., Danuor, S. K., Handwerker, J., Kohler, M., Lohon, M., Pedruzo-Bagazgoitia, X., Smith, V., Sunmonu, L., Wieser, A., Fink, A. H., and Knippertz, P.: An overview of the diurnal cycle of the atmospheric boundary layer during the West African monsoon season: results from the 2016 observational campaign, *Atmos. Chem. Phys.*, 18, 2913–2928, <https://doi.org/10.5194/acp-18-2913-2018>, 2018.
- 1145 Khairoutdinov, M. and Kogan, Y.: A New Cloud Physics Parameterization in a Large-Eddy Simulation Model of Marine Stratocumulus, *Mon. Weather Rev.*, 128, 229 – 243, [https://doi.org/10.1175/1520-0493\(2000\)128<0229:ANCPPI>2.0.CO;2](https://doi.org/10.1175/1520-0493(2000)128<0229:ANCPPI>2.0.CO;2), 2000.
- Knippertz, P., Fink, A. H., Schuster, R., Trentmann, J., Schrage, J. M., and Yorke, C.: Ultra-low clouds over the southern West African monsoon region, *Geophys. Res. Lett.*, 38, <https://doi.org/https://doi.org/10.1029/2011GL049278>, 2011.
- 1150 Knippertz, P., Coe, H., Chiu, J. C., Evans, M. J., Fink, A. H., Kalthoff, N., Liousse, C., Mari, C., Allan, R. P., Brooks, B., Danour, S., Flamant, C., Jegede, O. O., Lohou, F., and Marsham, J. H.: The DACCWA Project: Dynamics–Aerosol–Chemistry–Cloud Interactions in West Africa, *Bull. Amer. Meteor. Soc.*, 96, 1451 – 1460, <https://doi.org/10.1175/BAMS-D-14-00108.1>, 2015.
- 1155 Knippertz, P., Fink, A. H., Deroubaix, A., Morris, E., Tocquer, F., Evans, M. J., Flamant, C., Gaetani, M., Lavaysse, C., Mari, C., Marsham, J. H., Meynadier, R., Affo-Dogo, A., Bahaga, T., Brosse, F., Deetz, K., Guebsi, R., Latifou, I., Maranan, M., Rosenberg, P. D., and Schlueter, A.: A meteorological and chemical overview of the DACCWA field campaign in West Africa in June–July 2016, *Atmos. Chem. Phys.*, 17, 10893–10918, <https://doi.org/10.5194/acp-17-10893-2017>, 2017.
- Koch, D. and Del Genio, A. D.: Black carbon semi-direct effects on cloud cover: review and synthesis, *Atmos. Chem. Phys.*, 10, 7685–7696, <https://doi.org/10.5194/acp-10-7685-2010>, 2010a.
- 1160 Koch, D. and Del Genio, A. D.: Black carbon semi-direct effects on cloud cover: review and synthesis, *Atmos. Chem. Phys.*, 10, 7685–7696, <https://doi.org/10.5194/acp-10-7685-2010>, 2010b.
- Kreidenweis, S. M., Petters, M., and Lohmann, U.: 100 Years of Progress in Cloud Physics, Aerosols, and Aerosol Chemistry Research, *Meteorological Monographs*, 59, 11.1 – 11.72, <https://doi.org/10.1175/AMSMONOGRAPHS-D-18-0024.1>, 2019.
- 1165 Lac, C., Chaboureau, J.-P., Masson, V., Pinty, J.-P., Tulet, P., Escobar, J., Leriche, M., Barthe, C., Aouizerats, B., Augros, C., Aumond, P., Auguste, F., Bechtold, P., Berthet, S., Bielli, S., Bosseur, F., Caumont, O., Cohard, J.-M., Colin, J., Couvreux, F., Cuxart, J., Delautier, G., Dauhut, T., Ducrocq, V., Filippi, J.-B., Gazen, D., Geoffroy, O., Gheusi, F., Honnert, R., Lafore, J.-P., Lebeau-pin Brossier, C., Libois, Q., Lunet, T., Mari, C., Maric, T., Mascart, P., Mogé, M., Molinié, G., Nuissier, O., Pantillon, F., Peyrillé, P., Pergaud, J., Perraud, E., Pianezze, J., Redelsperger, J.-L., Ricard, D., Richard, E., Riette, S., Rodier, Q., Schoetter, R., Seyfried, L., Stein, J., Suhre, K., Taufour, M., Thouron, O., Turner, S., Verrelle, A., Vié, B., Visentin, F., Vionnet, V., and Wautelet, P.: Overview of the Meso-NH model version 5.4 and its applications, *Geoscientific Model Development*, 11, 1929–1969, <https://doi.org/10.5194/gmd-11-1929-2018>, 2018.
- 1175 ~~Lunet, T., Lac, C., Auguste, F., Visentin, F., Masson, V., and Escobar, J.: Combination of WENO and Explicit Runge–Kutta methods for wind transport in Meso-NH model, *Mon. Weather Rev.*, 145, 3817–3838, <https://doi.org/10.1175/MWR-D616-0343.12017>, 2017.~~

- Lascaux, F., Richard, E., and Pinty, J.-P.: Numerical simulations of three different MAP IOPs and the associated microphysical processes, *Quart. J. Roy. Meteorol. Soc.*, 132, 1907–1926, <https://doi.org/https://doi.org/10.1256/qj.05.197>, 2006.
- Legain, D., Bousquet, O., Douffet, T., Tzanos, D., Moulin, E., Barrie, J., and Renard, J.-B.: High-frequency boundary layer profiling with reusable radiosondes, *Atmospheric Measurement Techniques*, 6, 2195–2205, <https://doi.org/10.5194/amt-6-2195-2013>, 2013.
- Li, J., Carlson, B. E., Yung, Y. L., Lv, D., Hansen, J., Penner, J. E., Liao, H., Ramaswamy, V., Kahn, R. A., Zhang, P., Dubovik, O., Ding, A., Laciš, A. A., Zhang, L., and Dong, Y.: Scattering and absorbing aerosols in the climate system, *Nature Reviews Earth & Environment*, 3, 363–379, <https://doi.org/10.1038/s43017-022-00296-7>, 2022.
- Lioussé, C., Assamoi, E., Criqui, P., Granier, C., and Rosset, R.: Explosive growth in African combustion emissions from 2005 to 2030, *Environ. Res. Lett.*, 9, 035003, <https://doi.org/10.1088/1748-9326/9/3/035003>, 2014.
- Liu, Y., Jia, R., Dai, T., Xie, Y., and Shi, G.: A review of aerosol optical properties and radiative effects, *Journal of Meteorological Research*, 28, 1003–1028, <https://doi.org/10.1007/s13351-014-4045-z>, 2014.
- Lohmann, U. and Feichter, J.: Can the direct and semi-direct aerosol effect compete with the indirect effect on a global scale?, *Geophys. Res. Lett.*, 28, 159–161, <https://doi.org/https://doi.org/10.1029/2000GL012051>, 2001.
- Lohou, F., Kalthoff, N., Adler, B., Babic, K., Dione, C., Lathon, M., Pedruzo-Bagazgoitia, X., and Zouzoua, M.: Conceptual model of diurnal cycle of low-level stratiform clouds over southern West Africa, *Atmos. Chem. Phys.*, 20, 2263–2275, <https://doi.org/10.5194/acp-20-2263-2020>, 2020.
- Lunet, T., Lac, C., Auguste, F., Visentin, F., Masson, V., and Escobar, J.: Combination of WENO and Explicit Runge- Kutta methods for wind transport in Meso-NH model, *Mon. Weather Rev.*, 145, 3817–3838, <https://doi.org/10.1175/MWR-D616-0343.12017>, 2017.
- Mari, C., Evans, M. J., Palmer, P. I., Jacob, D. J., and Sachse, G. W.: Export of Asian pollution during two cold front episodes of the TRACE-P experiment, *J. Geophys. Res.-Atmos.*, 109, <https://doi.org/https://doi.org/10.1029/2003JD004307>, 2004.
- Mari, C. H., Cailley, G., Corre, L., Saunois, M., Attié, J. L., Thouret, V., and Stohl, A.: Tracing biomass burning plumes from the Southern Hemisphere during the AMMA 2006 wet season experiment, *Atmos. Chem. Phys.*, 8, 3951–3961, <https://doi.org/10.5194/acp-8-3951-2008>, 2008.
- Martcorena, B. and Bergametti, G.: Two-year simulations of seasonal and interannual changes of the Saharan dust emissions, *Geophys. Res. Lett.*, 23, 1921–1924, <https://doi.org/https://doi.org/10.1029/96GL01432>, 1996.
- Martin, G. M., Johnson, D. W., and Spice, A.: The Measurement and Parameterization of Effective Radius of Droplets in Warm Stratocumulus Clouds, *J. Atmos. Sci.*, 51, 1823 – 1842, [https://doi.org/10.1175/15200469\(1994\)051<1823:TMAPOE>2.0.CO;2](https://doi.org/10.1175/15200469(1994)051<1823:TMAPOE>2.0.CO;2), 1994.
- Masson, V., Le Moigne, P., Martin, E., Faroux, S., Alias, A., Alkama, R., Belamari, S., Barbu, A., Boone, A., Bouyssel, F., Brousseau, P., Brun, E., Calvet, J.-C., Carrer, D., Decharme, B., Delire, C., Donier, S., Essaouini, K., Gibelin, A.-L., Giordani, H., Habets, F., Jidane, M., Kerdraon, G., Kourzeneva, E., Lafaysse, M., Lafont, S., Lebeaupin Brossier, C., Lemonsu, A., Mahfouf, J.-F., Marguinaud, P., Mokhtari, M., Morin, S., Pigeon, G., Salgado, R., Seity, Y., Taillefer, F., Tanguy, G., Tulet, P., Vincendon, B., Vionnet, V., and Voldoire, A.: The SURFEXv7.2 land and ocean surface platform for coupled or offline simulation of earth surface variables and fluxes, *Geoscientific Model Development*, 6, 929–960, <https://doi.org/10.5194/gmd-6-929-2013>, 2013.
- Menut, L., Flamant, C., Turquety, S., Deroubaix, A., Chazette, P., and Meynadier, R.: Impact of biomass burning on pollutant surface concentrations in megacities of the Gulf of Guinea, *Atmos. Chem. Phys.*, 18, 2687–2707, <https://doi.org/10.5194/acp18-2687-2018>, 2018.
- Menut, L., Tuccella, P., Flamant, C., Deroubaix, A., and Gaetani, M.: The role of aerosol–radiation–cloud interactions in linking anthropogenic pollution over southern west Africa and dust emission over the Sahara, *Atmos. Chem. Phys.*, 19, 14657–14676, <https://doi.org/10.5194/acp-19-14657-2019>, 2019.
- Metzger, S., Dentener, F., Pandis, S., and Lelieveld, J.: Gas/aerosol partitioning: 1. A computationally efficient model, *J. Geophys. Res.-Atmos.*, 107, ACH 16–1–ACH 16–24, <https://doi.org/https://doi.org/10.1029/2001JD001102>, 2002.

- 1225 Mlawer, E. J., Taubman, S. J., Brown, P. D., Iacono, M. J., and Clough, S. A.: Radiative transfer for inhomogeneous atmospheres: RRTM, a validated correlated-k model for the longwave, *J. Geophys. Res.-Atmos.*, 102, 16663–16682, <https://doi.org/https://doi.org/10.1029/97JD00237>, 1997.
- Morcrette, J.-J.: The Surface Downward Longwave Radiation in the ECMWF Forecast System, *J. Clim.*, 15, 1875 – 1892, [https://doi.org/10.1175/1520-0442\(2002\)015<1875:TSDLRI>2.0.CO;2](https://doi.org/10.1175/1520-0442(2002)015<1875:TSDLRI>2.0.CO;2), 2002.
- 1230 Murphy, J. G., Oram, D. E., and Reeves, C. E.: Measurements of volatile organic compounds over West Africa, *Atmos. Chem. Phys.*, 10, 5281–5294, <https://doi.org/10.5194/acp-10-5281-2010>, 2010.
- Noilhan, J. and Planton, S.: A Simple Parameterization of Land Surface Processes for Meteorological Models, *Mon. Weather Rev.*, 117, 536 – 549, [https://doi.org/10.1175/1520-0493\(1989\)117<0536:ASPOLS>2.0.CO;2](https://doi.org/10.1175/1520-0493(1989)117<0536:ASPOLS>2.0.CO;2), 1989.
- 1235 Pedruzo-Bagazgoitia, X., de Roode, S. R., Adler, B., Babic, K., Dione, C., Kalthoff, N., Lohou, F., Lothon, M., and Vilà-Guerau de Arellano, J.: The diurnal stratocumulus-to-cumulus transition over land in southern West Africa, *Atmos. Chem. Phys.*, 20, 2735–2754, <https://doi.org/10.5194/acp-20-2735-2020>, 2020.
- Petters, J. L., Harrington, J. Y., and Clothiaux, E. E.: Radiative–dynamical feedbacks in low liquid water path stratiform clouds, *J. Atmos. Sci.*, 69, 1498-1512, <https://doi.org/10.1175/JAS-D-11-0169.1>, 2012
- 1240 Pinty, J.-P. and Jabouille, P.: A mixed-phased cloud parameterization for use in a mesoscale non-hydrostatic model: simulations of a squall line and of orographic precipitation, *Proc. Conf. on Cloud Physics*, 217–220. 1998.
- Pruppacher, H. R., Klett, J. D., and Wang, P. K.: Microphysics of Clouds and Precipitation, *Aerosol Science and Technology*, 28, 381–382, <https://doi.org/10.1080/02786829808965531>, 1998.
- Reeves, C. E., Formenti, P., Afif, C., Ancellet, G., Attié, J.-L., Bechara, J., Borbon, A., Cairo, F., Coe, H., Crumeyrolle, S., Fierli, F., Flamant, C., Gomes, L., Hamburger, T., Lambert, C., Law, K. S., Mari, C., Jones, R. L., Matsuki, A., Mead, 1245 M. I., Methven, J., Mills, G. P., Minikin, A., Murphy, J. G., Nielsen, J. K., Oram, D. E., Parker, D. J., Richter, A., Schlager, H., Schwarzenboeck, A., and Thouret, V.: Chemical and aerosol characterisation of the troposphere over West Africa during the monsoon period as part of AMMA, *Atmos. Chem. Phys.*, 10, 7575–7601, <https://doi.org/10.5194/acp-10-7575-2010>, 2010.
- 1250 Sandu, I., Brenguier, J.-L., Geoffroy, O., Thouron, O., and Masson, V.: Aerosol Impacts on the Diurnal Cycle of Marine Stratocumulus, *J. Atmos. Sci.*, 65, 2705 – 2718, <https://doi.org/10.1175/2008JAS2451.1>, 2008.
- Sauvage, B., Thouret, V., Cammas, J.-P., Gheusi, F., Athier, G., and Nédélec, P.: Tropospheric ozone over Equatorial Africa: regional aspects from the MOZAIC data, *Atmos. Chem. Phys.*, 5, 311–335, <https://doi.org/10.5194/acp-5-311-2005>, 2005.
- 1255 Schrage, J. M. and Fink, A. H.: Nocturnal Continental Low-Level Stratus over Tropical West Africa: Observations and Possible Mechanisms Controlling Its Onset, *Mon. Weather Rev.*, 140, 1794 – 1809, <https://doi.org/10.1175/MWR-D-11-00172.1>, 2012.
- Schuster, R., Fink, A. H., and Knippertz, P.: Formation and maintenance of nocturnal low-level stratus over the Southern West African monsoon region during AMMA 2006, *J. Atmos. Sci.*, 70, 2337 – 2355, <https://doi.org/10.1175/JAS-D-120241.1>, 2013.
- 1260 Stevens, B., Cotton, W. R., Feingold, G., and Moeng, C.-H.: Large-eddy simulations of strongly precipitating, shallow, stratocumulus-topped boundary layers, *J. Atmos. Sci.*, 55, 3616-3638, 1998.
- Stevens, B., Moeng, C.-H., Ackerman, A. S., Bretherton, C. S., Chlond, A., de Roode, S., Edwards, J., Golaz, J.-C., Jiang, H., Khairoutdinov, M., Kirkpatrick, M. P., Lewellen, D. C., Lock, A., Müller, F., Stevens, D. E., Whelan, E., and Zhu, 1265 P.: Evaluation of large-eddy simulations via observations of nocturnal marine stratocumulus, *Mon. Weather Rev.*, 133, 1443–1462, <https://doi.org/10.1175/MWR2930.1>, 2005.
- Stjern, C. W., Samset, B. H., Myhre, G., Forster, P. M., Hodnebrog, , Andrews, T., Boucher, O., Faluvegi, G., Iversen, T., Kasoar, M., Kharin, V., Kirkevåg, A., Lamarque, J.-F., Olivie, D., Richardson, T., Shawki, D., Shindell, D., Smith, C. J., Takemura, T., and Voulgarakis, A.: Rapid adjustments cause weak surface temperature response to increased black carbon concentrations, *J. Geophys. Res.-Atmos.*, 122, 11,462–11,481, <https://doi.org/https://doi.org/10.1002/2017JD027326>, 2017.
- 1270 Taylor, J. W., Haslett, S. L., Bower, K., Flynn, M., Crawford, I., Dorsey, J., Choularton, T., Connolly, P. J., Hahn, V., Voigt, C., Sauer, D., Dupuy, R., Brito, J., Schwarzenboeck, A., Bourriane, T., Denjean, C., Rosenberg, P., Flamant, C., Lee, J. D., Vaughan, A. R., Hill, P. G., Brooks, B., Catoire, V., Knippertz, P., and Coe, H.: Aerosol influences on low-level

- clouds in the West African monsoon, *Atmos. Chem. Phys.*, 19, 8503–8522, <https://doi.org/10.5194/acp-19-8503-2019>, 2019.
- 1275 Thouron, O., Brenguier, J.-L., and Burnet, F.: Supersaturation calculation in large eddy simulation models for prediction of the droplet number concentration, *Geoscientific Model Development*, 5, 761–772, <https://doi.org/10.5194/gmd-5-761-2012>, 2012.
- 1280 Tulet, P., Crassier, V., Solmon, F., Guedalia, D., and Rosset, R.: Description of the mesoscale nonhydrostatic chemistry model and application to a transboundary pollution episode between northern France and southern England, *J. Geophys. Res.-Atmos.*, 108, ACH 5–1–ACH 5–11, <https://doi.org/https://doi.org/10.1029/2000JD000301>, 2003.
- Tulet, P., Crassier, V., Cousin, F., Suhre, K., and Rosset, R.: ORILAM, a three-moment lognormal aerosol scheme for mesoscale atmospheric model: Online coupling into the Meso-NH-C model and validation on the Escompte campaign, *J. Geophys. Res.-Atmos.*, 110, <https://doi.org/10.1029/2004JD005716>, 2005.
- 1285 Tulet, P., Grini, A., Griffin, R. J., and Petitcol, S.: ORILAM-SOA: A computationally efficient model for predicting secondary organic aerosols in three-dimensional atmospheric models, *J. Geophys. Res.-Atmos.*, 111, <https://doi.org/10.1029/2006JD007152>, 2006.
- 1290 Twohy, C. H., Anderson, J. R., Toohey, D. W., Andrejczuk, M., Adams, A., Lytle, M., George, R. C., Wood, R., Saide, P., Spak, S., Zuidema, P., and Leon, D.: Impacts of aerosol particles on the microphysical and radiative properties of stratocumulus clouds over the southeast Pacific Ocean, *Atmos. Chem. Phys.*, 13, 2541–2562, <https://doi.org/10.5194/acp-13-2541-2013>, 2013.
- Twomey, S.: PRECIPITATION BY DIRECT INTERCEPTION OF CLOUD-WATER, *Weather*, 12, 120–122, <https://doi.org/https://doi.org/10.1002/j.1477-8696.1957.tb00453.x>, 1957.
- 1295 Van der Dussen, J. J., de Roode, S. R., and Siebesma, A. P.: Factors controlling rapid stratocumulus cloud thinning, *J. Atmos. Sci.*, 71, 655–664, <https://doi.org/10.1175/JAS-D-13-0114.1>, 2014.
- Vié, B., Pinty, J.-P., Berthet, S., and Leriche, M.: LIMA (v1.0): A quasi two-moment microphysical scheme driven by a multimodal population of cloud condensation and ice freezing nuclei, *Geoscientific Model Development*, 9, 567–586, <https://doi.org/10.5194/gmd-9-567-2016>, 2016.
- 1300 Wang, S., Wang, Q., and Feingold, G.: Turbulence, Condensation, and Liquid Water Transport in Numerically Simulated Nonprecipitating Stratocumulus Clouds, *J. Atmos. Sci.*, 60, 262–278, [https://doi.org/10.1175/1520-0469\(2003\)060<0262:TCALWT>2.0.CO;2](https://doi.org/10.1175/1520-0469(2003)060<0262:TCALWT>2.0.CO;2), 2003.
- Wood, R.: Stratocumulus Clouds, *Mon. Weather Rev.*, 140, 2373 – 2423, <https://doi.org/10.1175/MWR-D-11-00121.1>, 2012.
- 1305 Yamaguchi, T., Feingold, G., Kazil, J., and McComiskey, A.: Stratocumulus to cumulus transition in the presence of elevated smoke layers, *Geophys. Res. Lett.*, 42, 10,478–10,485, <https://doi.org/https://doi.org/10.1002/2015GL066544>, 2015.
- Zhang, J. and Zuidema, P.: The diurnal cycle of the smoky marine boundary layer observed during August in the remote southeast Atlantic, *Atmos. Chem. Phys.*, 19, 14493–14516, <https://doi.org/10.5194/acp-19-14493-2019>, 2019.
- 1310 Zouzoua, M., Lohou, F., Assamoi, P., Lathon, M., Yoboue, V., Dione, C., Kalthoff, N., Adler, B., Babic, K., Pedruzo-Bagazgoitia, X., and Derrien, S.: Breakup of nocturnal low-level stratiform clouds during the southern West African monsoon season, *Atmos. Chem. Phys.*, 21, 2027–2051, <https://doi.org/10.5194/acp-21-2027-2021>, 2021.